Supporting Information

Triple–Readout Luminescence Thermometry in a Heterodinuclear Yb-Er Complex and Performance Comparison with the Homodinuclear Analogues

Yolimar Gil,[a]* Julio Corredoira-Vázquez,[b,c] Ricardo Costa de Santana,[d] Andres Vega,[e] Albano N. Carneiro Neto,[f,g] Daniel Aravena,[h] Evgenia Spodine,[a] Carlos D. S. Brites,[f] Luís D. Carlos,*[f] Pablo Fuentealba[a]*.

[a] *Facultad de Ciencias Químicas y Farmacéuticas, Universidad de Chile, Olivos 1007, 8380544, Santiago, Chile. E-mail: yolimar.gil@ciq.uchile.cl*

[b] *Departamento de Química Inorgánica, Facultade de Química, Universidade de Santiago de Compostela, 15782 Santiago de Compostela, Spain.*

[c] *Institute of Materials (iMATUS), Universidade de Santiago de Compostela, 15782 Santiago de Compostela, Spain.*

[d] *Instituto de Física, Universidade Federal de Goiás, Campus Samambaia, 74690-900, Goiânia, GO, Brazil.*

[e] *Departamento de Ciencias Químicas, Universidad Andrés Bello, Av. República 275, 8370011, Santiago, Chile.*

[f] *Phantom-g, CICECO – Aveiro Institute of Materials, Department of Physics, University of Aveiro, 3810-193 – Aveiro, Portugal. E-mail: lcarlos@ua.pt*

[g] *Department of Molecular Theory and Spectroscopy, Max Planck Institut für Kohlenforschung, Mülheim an der Ruhr D-45470, Germany.*

[h] *Departamento de Química de los Materiales, Facultad de Química y Biología, Universidad de Santiago de Chile, Casilla 40, Correo 33, Santiago, Chile*

Contents

1. Synthesis and molecular characterization .2
Figure S1. 3
Figure S2 4
2. Structural Characterization 4
Scheme S1 4
Figure S3. 5
Table S1 6
Table S2 7
Table S3 7
Table S4 8
Figure S4 8
Figure S5 9
Table S5 9
Figure S6 10
Figure S7. 12
Figure S8 13
Figure S9 13
Figure S10. 14
Table S6. 14
Figure S11 15
Figure S12 16
3. Photoluminescence Characterization 17
Figure S13 17
Figure S14 17
Figure S15 18
4. Thermometric Characterization 18
Figure S16 19
Figure S17 19

Figure S18 20
Figure S19 20
Figure S20 21
Table S7.....22
5. Theoretical calculations.....23
Figure S21. 23
Figure S22. 24
Table S8.....25
Figure S23. 25
Figure S24. 27
Table S9.....30
Table S10.....31
Table S11.....32
Table S12.....32
Figure S25. 33
Figure S26. 33
Table S13.....34
Figure S27. 36
Figure S28. 37
Figure S29. 37
References 38

1. Synthesis and molecular characterization

Synthesis of Homodinuclear [{Ln(tta)$_3$}$_2$(μ^2-bpm)] (Ln = Yb^{3+} (2), Er^{3+} (3)). In a 30-mL volume microwave vial, 2-thenoyltrifluoro-acetone (267 mg, 1.2 mmol) was dissolved in 15 mL of methanol:ethanol mixture (1:1). Then, triethylamine (168μL, 1.2 mmol) and Ln(NO$_3$)$_3$.6H$_2$O (180 mg (Ln^{3+} : Yb) or 177 mg (Ln^{3+} : Er), 0.4 mmol) were added and the mixture was stirred for 15 min. Finally, a solution of bpm (31.6 mg, 0.2 mmol) in 5 mL of the same solvent mixture was added, and the resulting solution was irradiated in the microwave reactor for 15 min at 100 ° (See Figure S1 for the full reaction profiles recorded by the instrument). X-ray single crystals were obtained by slow evaporation of the reaction solutions after 4 days. Pale yellow rods were obtained for [{Yb(tta)$_3$}$_2$(μ^2-bpm)](**2**) with a yield of 265mg (72.4%), while [{Er(tta)$_3$}$_2$(μ^2-bpm)] (**3**) afforded pale pink blocks with a yield of 285mg (78.3%). Anal. calc. for **2**: $C_{56}H_{30}F_{18}N_4O_{12}S_6Yb_2$: C, 36.73; H, 1.65; N, 3.06 %. Found C, 36.44; H, 1.76; N, 3.13 %. Anal. calc. for **3**: $C_{56}H_{30}Er_2F_{18}N_4O_{12}S_6$: C, 36.96; H, 1.66; N, 3.08 %. Found C, 36.91; H, 1.79; N, 3.15 %. ESI-MS for **2**: m/z = 1849.8982 $[M+NH_4]^+$, and for **3**: m/z = 1837.8793 $[M+NH_4]^+$.

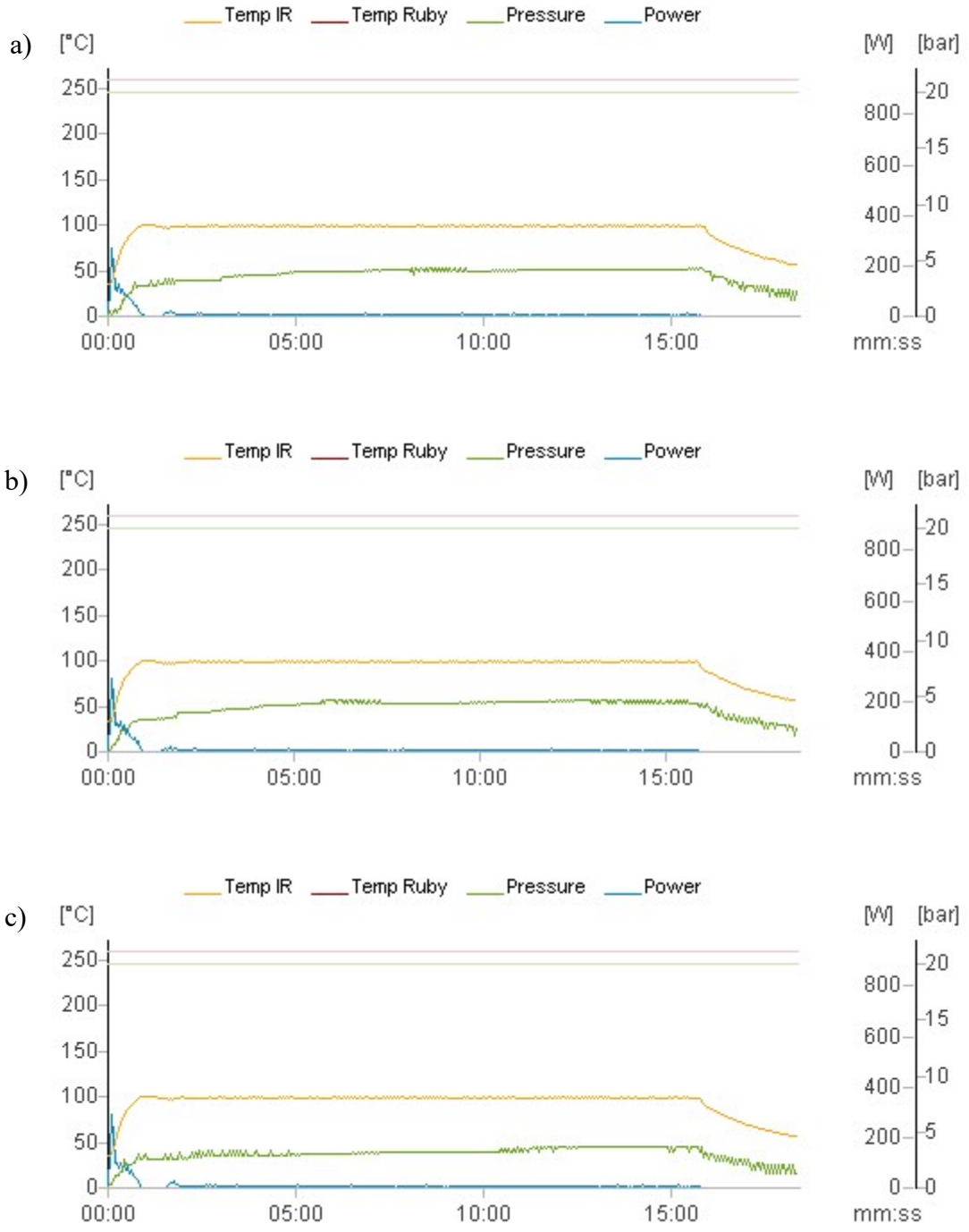

Figure S1. Temperature, applied power, and internal pressure profiles recorded during the microwave-assisted synthesis performed at a target temperature of 100 °C for 15 min for **1** (a), **2** (b) and **3** (c).

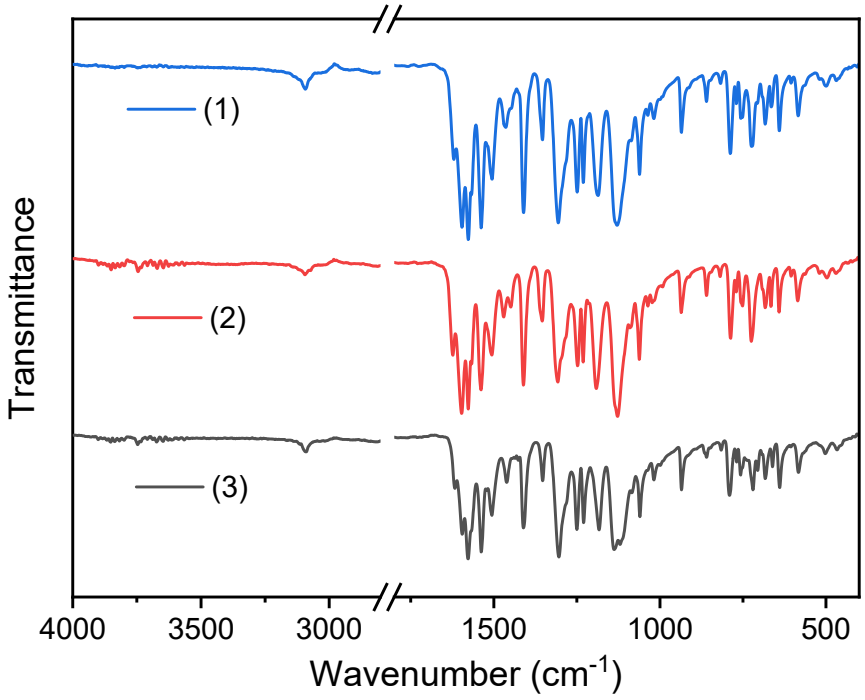

Figure S2. FTIR spectra for **1-3** complexes.

2. Structural Characterization

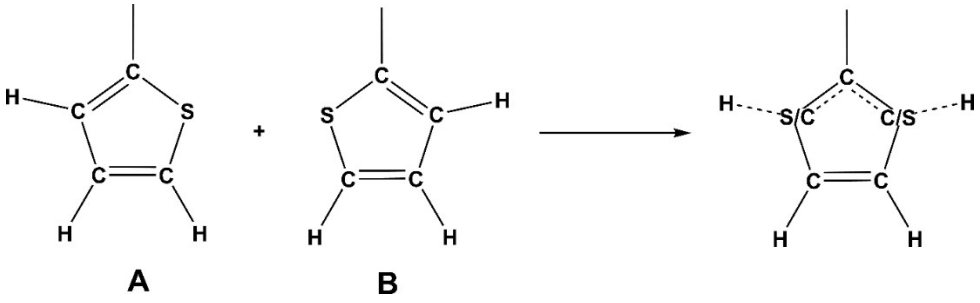

Scheme S1. Disorder on the thiophenyl groups.

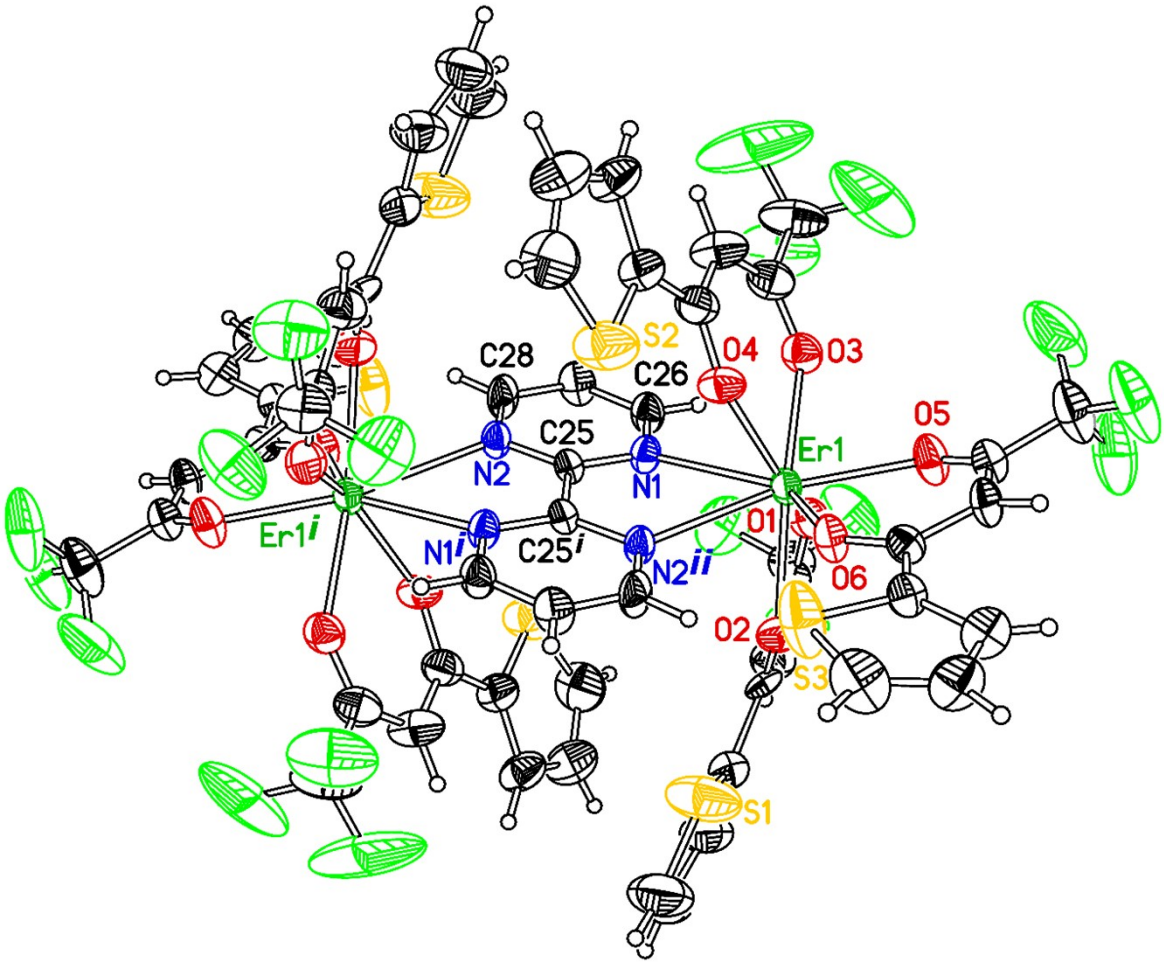

Figure S3. Molecular structure of **3** determined by single crystal X-rays diffraction. Displacement ellipsoids drawn at the 50% level of probability. Hydrogen atoms drawn as arbitrary radii spheres. Symmetry label: i: 1 - x, 1 - y, 1 - z.

Table S1. Crystal data and structure refinement details for **1** and **3**.

	1	**3**
CSD Deposit Code	CCDC2338183	CCDC2419767
FW/uma	1819.72	909.86
Formula	$C_{56}H_{30}ErF_{18}N_4O_{12}S_6Yb$	$C_{28}H_{15}ErF_9N_2O_6S_3$
T / K	296	296
Crystal System	Monoclinic	Monoclinic
Space Group	$P2_1/n$	$P2_1/c$
a (Å)	13.6707(14)	10.3989(4)
b (Å)	14.1628(14)	21.6815(8)
c (Å)	17.7737(19)	14.8024(5)
α (°)	90	90
β (°)	97.682(4)	106.318(1)
γ (°)	90	90
V (Å ^{3})	3410.4(6)	3203.0(2)
Z(Z')	2(2)	2(4)
d (g cm^{-3})	1.766	1.887
μ (mm^{-1})	2.74	2.91
F(000)	1768.0	1768.0
θ range	1.80 to 26.0	1.70 to 26.0
hkl range	$-16 \leq h \leq 16$	$-12 \leq h \leq 12$
	$-17 \leq k \leq 17$	$-26 \leq k \leq 26$
	$-21 \leq l \leq 21$	$-18 \leq l \leq 18$
N_{tot}, N_{uniq} (R_{int}), N_{obs}	25831, 6686(0.140), 3124	24746, 6291(0.028), 5904
Ref. Parameters	553	442
GOF	1.01	1.45
R_1, wR_2 (obs)	0.060, 0.194	0.061, 0.119
Max. and min Δρ e Å^{-3}	1.01, -1.59	1.29, -2.66

Table S2. Selected bonds (Å) and angles (°) for **1**.

Er1—O3	2.251(8)	Er1—O1	2.279(8)
Er1—O4	2.255(8)	Er1—O6	2.287(7)
Er1—O2	2.262(8)	Er1—N1	2.540(9)
Er1—O5	2.264(7)	Er1—N2^{i}	2.544(10)
O3—Er1—O4	74.7(3)	O5—Er1—O6	73.6(3)
O3—Er1—O2	86.2(3)	O1—Er1—O6	139.3(3)
O4—Er1—O2	76.2(3)	O3—Er1—N1	145.7(3)
O3—Er1—O5	75.6(3)	O4—Er1—N1	139.4(3)
O4—Er1—O5	120.2(3)	O2—Er1—N1	103.3(3)
O2—Er1—O5	149.9(3)	O5—Er1—N1	80.6(3)
O3—Er1—O1	78.7(3)	O1—Er1—N1	72.8(3)
O4—Er1—O1	140.9(3)	O6—Er1—N1	73.5(3)
O2—Er1—O1	73.9(3)	O3—Er1—N2^{i}	147.8(3)
O5—Er1—O1	79.1(3)	O4—Er1—N2^{i}	78.5(3)
O3—Er1—O6	121.4(3)	O2—Er1—N2^{i}	70.2(3)
O4—Er1—O6	79.6(3)	O5—Er1—N2^{i}	134.5(3)
O2—Er1—O6	136.4(3)	O1—Er1—N2^{i}	113.4(3)
N1—Er1—N2^{i}	64.0(3)	O6—Er1—N2^{i}	69.8(3)

Symmetry label: ***i:*** *-x, -y, -z.*

Table S3. Selected bonds (Å) and angles (°) for **3**.

Er1—O5	2.261(5)	Er1—O6	2.314(5)
Er1—O4	2.282(6)	Er1—O3	2.314(6)
Er1—O1	2.299(6)	Er1—N1	2.578(6)
Er1—O2	2.303(6)	Er1—N2^{i}	2.612(6)
O5—Er1—O4	104.5(2)	O6—Er1—O3	130.2(2)
O5—Er1—O1	87.2(2)	O5—Er1—N1	146.93(19)
O4—Er1—O1	143.5(2)	O4—Er1—N1	78.3(2)
O5—Er1—O2	103.9(2)	O1—Er1—N1	73.9(2)
O4—Er1—O2	134.0(2)	O2—Er1—N1	96.2(2)
O1—Er1—O2	72.9(2)	O6—Er1—N1	137.57(19)
O5—Er1—O6	73.61(19)	O3—Er1—N1	73.5(2)
O4—Er1—O6	78.0(2)	O5—Er1—N2^{i}	149.87(19)
O1—Er1—O6	138.3(2)	O4—Er1—N2^{i}	67.5(2)
O2—Er1—O6	76.3(2)	O1—Er1—N2^{i}	116.9(2)
O5—Er1—O3	76.0(2)	O2—Er1—N2^{i}	69.7(2)
O4—Er1—O3	72.7(2)	O6—Er1—N2^{i}	76.28(18)
O1—Er1—O3	77.1(2)	O3—Er1—N2^{i}	124.67(19)
O2—Er1—O3	150.0(2)	N1—Er1—N2^{i}	62.24(19)

Symmetry label: ***i****: 1 - x, 1 - y, 1 - z.*

Table S4. The CShM values calculated by SHAPE 2.1 for **1** and [{Yb(tta)$_3$}$_2$(μ^2-bpm)].[1]

Coordination Geometry	**1**	[{Yb(tta)$_3$}$_2$(μ^2-bpm)]
Octagon (D_{8h})	29.420	29.739
Heptagonal pyramid (C_{7v})	21.867	21.755
Hexagonal bipyramid (D_{6h})	16.274	16.402
Cube (O_h)	9.537	9.921
Square antiprism (D_{4d})	**0.538**	**0.424**
Triangular dodecahedron (D_{2d})	2.185	2.596
Johnson gyrobifastigium J26 (D_{2d})	15.715	16.966
Johnson elongated triangular bipyramid J14 (D_{3h})	27.973	28.188
Biaugmented trigonal prism J50 (C_{2v})	2.377	2.968
Biaugmented trigonal prism (C_{2v})	1.831	2.337
Snub diphenoid J84 (D_{2d})	5.032	5.559
Triakis tetrahedron (T_d)	10.289	10.756
Elongated trigonal bipyramid (D_{3h})	23.907	24.573

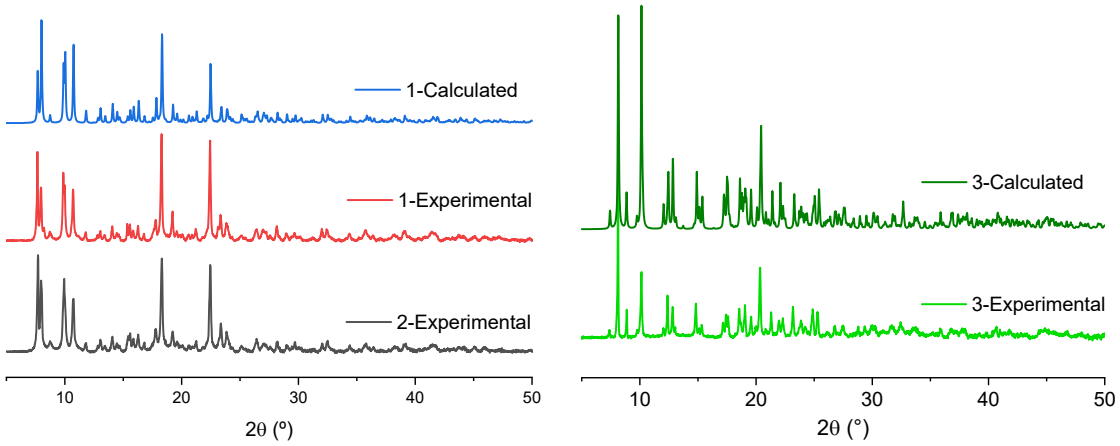

Figure S4. Comparison between experimental and calculated powder X-ray diffraction (PXRD) patterns for 1 and 2 (left panel) and 3 (right panel).

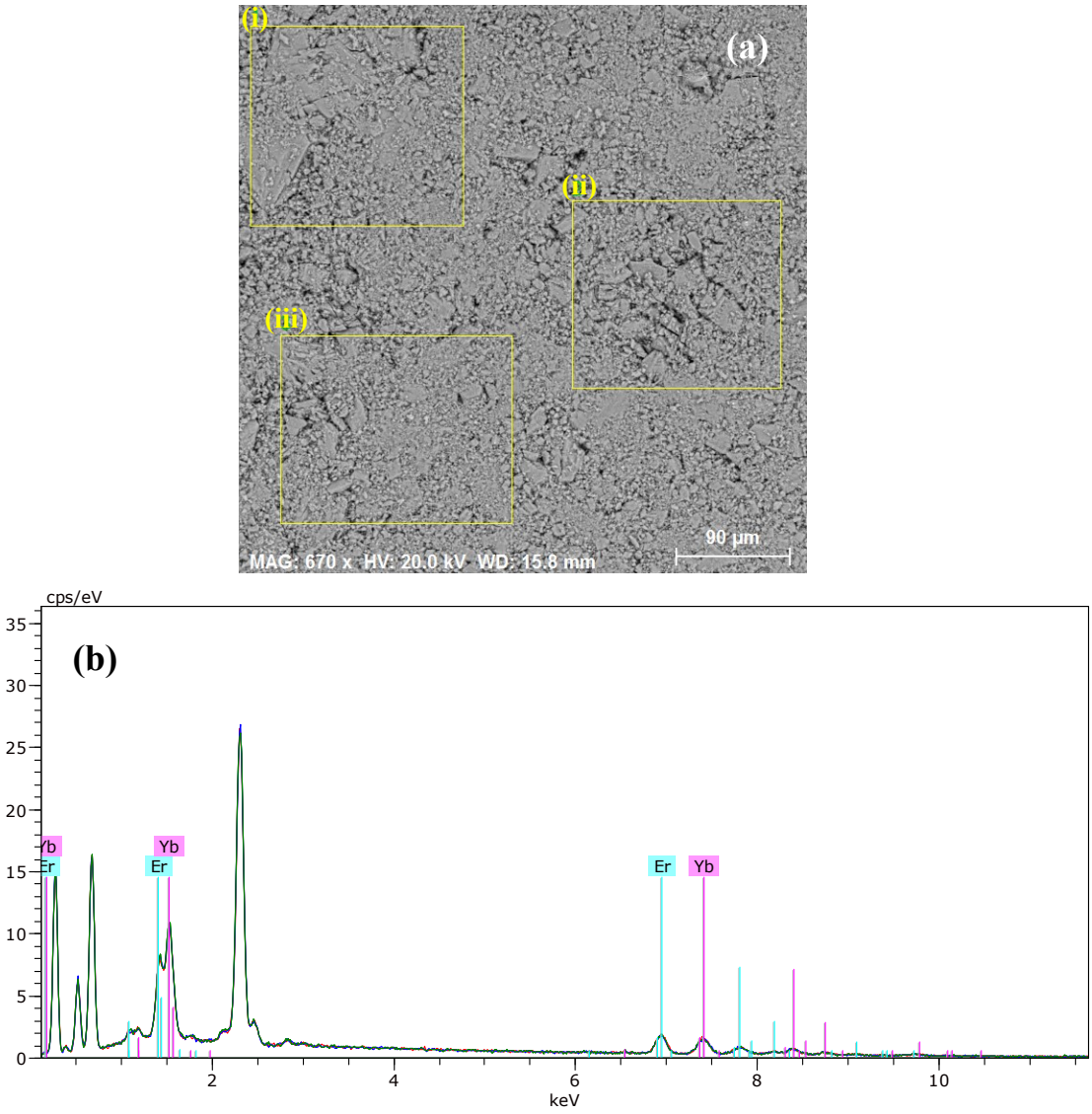

Figure S5. (a) SEM image for **1** displaying three selected areas and the corresponding (b) EDX spectrum for these areas: i(blue), ii(red) and iii(green).

Table S5. EDX determination of mass percent (%) of Yb^{3+} and Er^{3+} in **1**.

Spectrum	Mass percent (%)	
	Er^{3+}	Yb^{3+}
1	48.04	51.96
2	50.18	49.82
3	50.19	49.81
Mean value	49.47	50.53
Sigma	1.24	1.24
Sigma mean	0.72	0.72

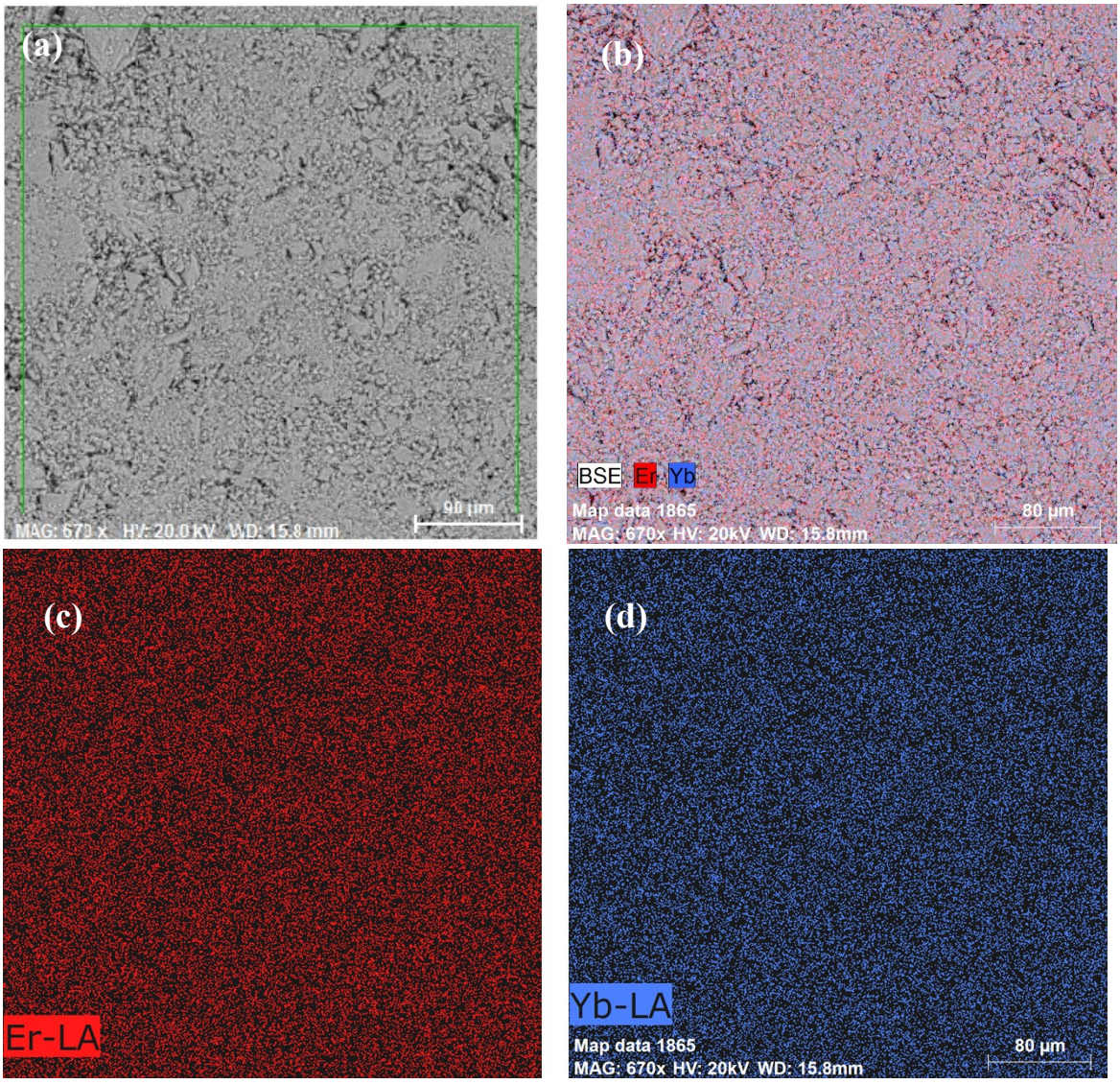

Figure S6. (a) SEM image and (b-d) SEM-EDX mapping of **1**.

Electrospray ionization mass spectrometry (ESI-MS)

The MS measurements were performed under soft ionization conditions (fragmentation energy of 10 eV), selected to preserve the molecular ion. For all the reported complexes, the ESI-MS spectra display signals corresponding to the isotopic distribution of the dinuclear species, detected as the ammonium adduct $[M + NH_4]^+$: m/z 1841.8802 (**1**), 1849.8982 (**2**), and 1837.8793 (**3**) (Figure S7-S9). The observation of these dinuclear signals confirms the integrity of the dinuclear complexes under the applied ionization conditions, although it does not constitute direct evidence of their thermodynamic stability in solution.

For clarity, a full ESI-MS spectrum of **1** is shown in Figure S10 and peak assignments are summarized in Table S6. In addition to the molecular ion of the heterodinuclear complex (**1**), detected as the ammonium adduct $[M + NH_4]^+$, several intense lower-m/z signals are observed and can be rationalized in terms of stepwise fragmentation of the heterodinuclear complex under the applied ESI conditions (see Experimental Section). A prominent fragment at m/z 1602.8569 (relative intensity 63.9%) is assigned to the heterodinuclear complex after the loss of one tta ligand, consistent with partial ligand dissociation while preserving the dinuclear metal framework. At lower m/z, an intense peak at m/z 1006.9833 (relative intensity 77.1%) is tentatively assigned to the mononuclear fragment $[Er(bpm)(tta)_3 + NH_4]^+$, arising from further dissociation of the dinuclear complex. Finally, the signal at m/z 767.9617 (relative intensity 35.7%) is tentatively attributed to the cationic fragment $[Er(bpm)(tta)_2]^+$. The relative intensities of these peaks are influenced by ionization and fragmentation processes and should therefore not be interpreted quantitatively.

A comparison of the isotopic patterns in the molecular-ion region of the heterodinuclear complex **1** and the corresponding homodinuclear analogues **2** and **3** are shown in Figure S11, together with the calculated isotopic distribution for the $[M + NH_4]^+$ ion of **1**. The experimental isotopic envelope of **1** shows excellent agreement with the calculated pattern and is clearly dominated by the heterodinuclear species. Minor contributions matching the isotopic pattern of the homodinuclear complexes are only observed in the expanded region. Such minor features have been reported for related heterodinuclear lanthanide coordination assemblies and have been attributed to partial metal-ion scrambling processes associated with the intrinsic lability of Ln-ligand interactions.[2, 3] The comparison further supports the

assignment of the heterodinuclear complex and illustrates the sensitivity of ESI-MS to detect closely related dinuclear species.

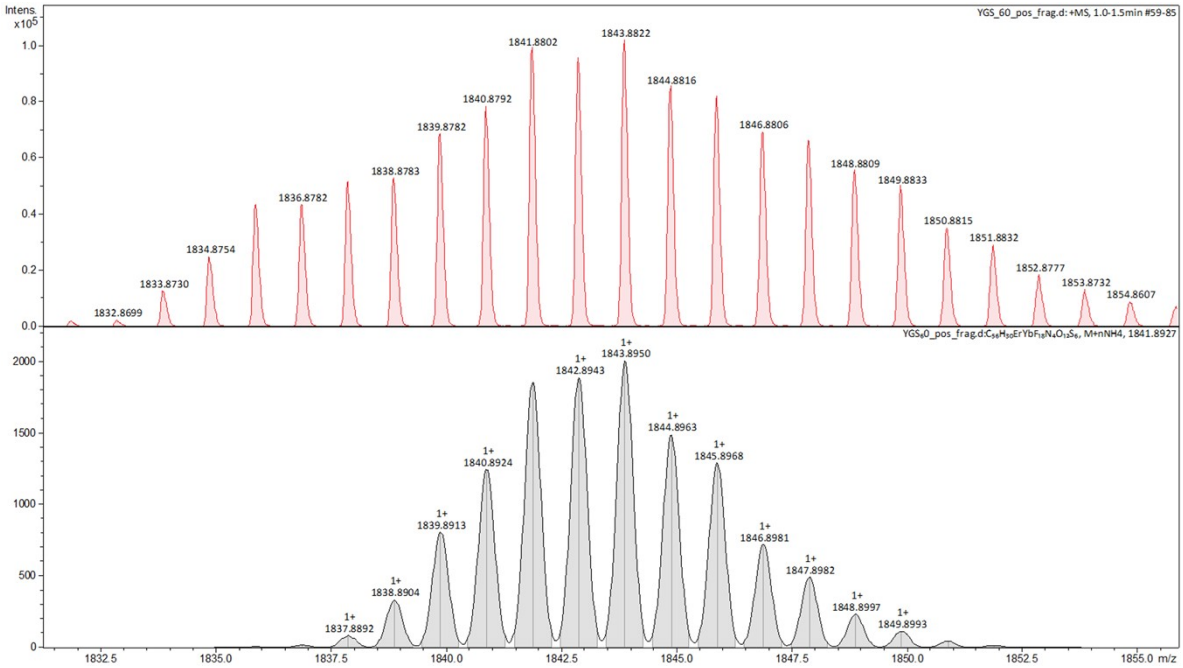

Figure S7. Selected region of the experimental ESI-MS spectra of compound **1** (top), and calculated signals corresponding to $[M+NH_4]^+$ ion (bottom).

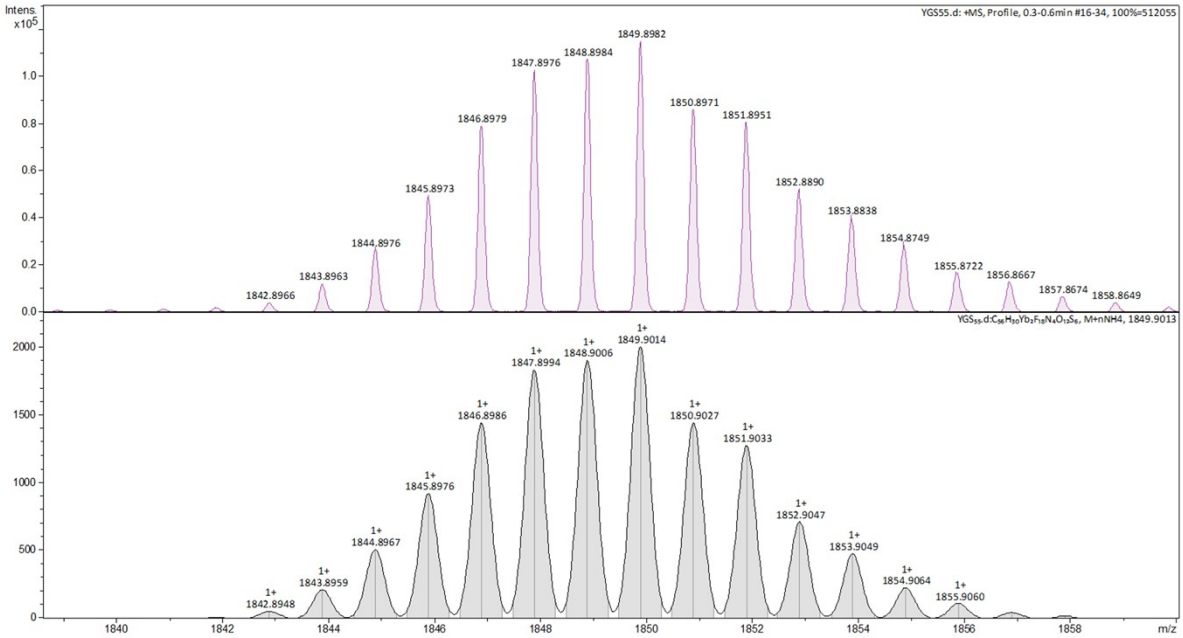

Figure S8. Selected region of the experimental ESI-MS spectra of compound **2** (top), and calculated signals corresponding to $[M+NH_4]^+$ ion (bottom).

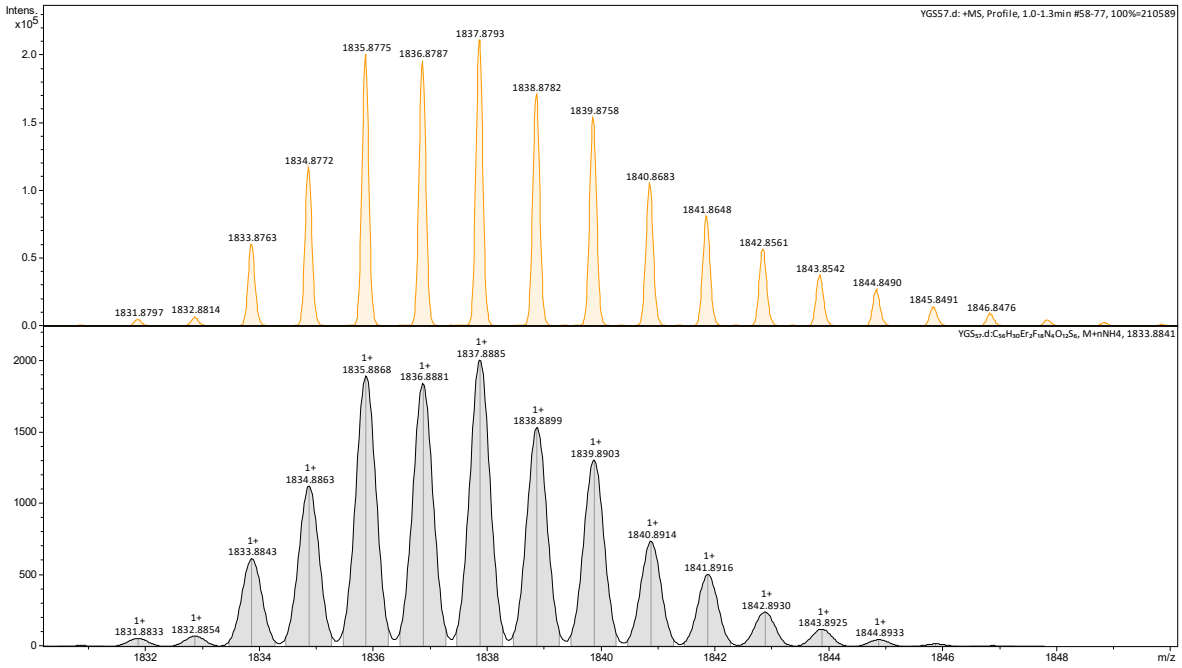

Figure S9. Selected region of the experimental ESI-MS spectra of compound **3** (top), and calculated signals corresponding to $[M+NH_4]^+$ ion (bottom).

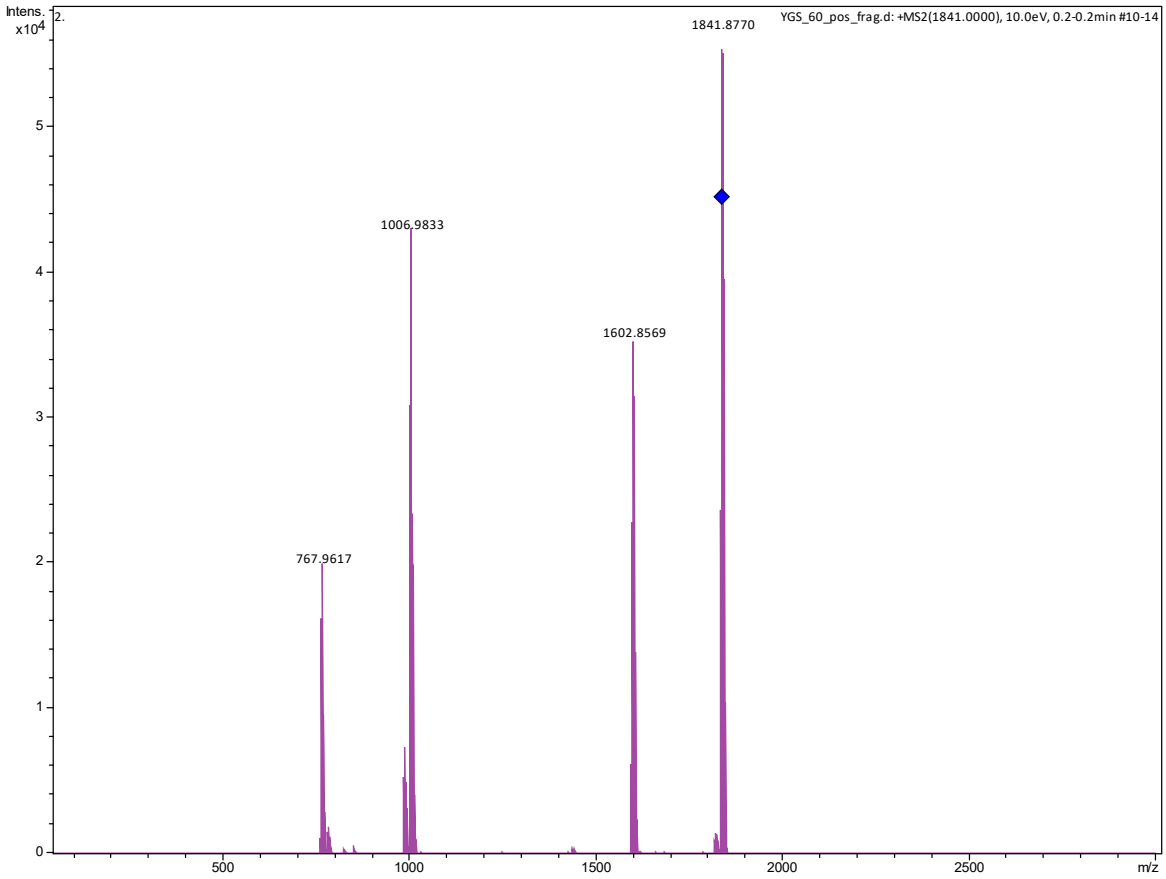

Figure S10. Full ESI-MS spectrum of **1** recorded under soft ionization conditions (fragmentation energy of 10 eV). The main observed peaks and their assignments are summarized in Table S6.

Table S6. Observed *m/z* values, relative intensities, and tentative assignments of the main ions detected in the ESI-MS spectrum of **1**.

m/z (obs.)	Assignment	Relative intensity (%)
1841.8770	$[M + NH_4]^+$	100
1602.8569	$[M - tta]^+$	63.9
1006.9833	$[Er(bpm)(tta)_3 + NH_4]^+$	77.1
767.9617	$[Er(bpm)(tta)_2]^+$	35.7

M denotes the heterodinuclear complex [{Yb(tta)₃}(μ₂-bpm){Er(tta)₃}].

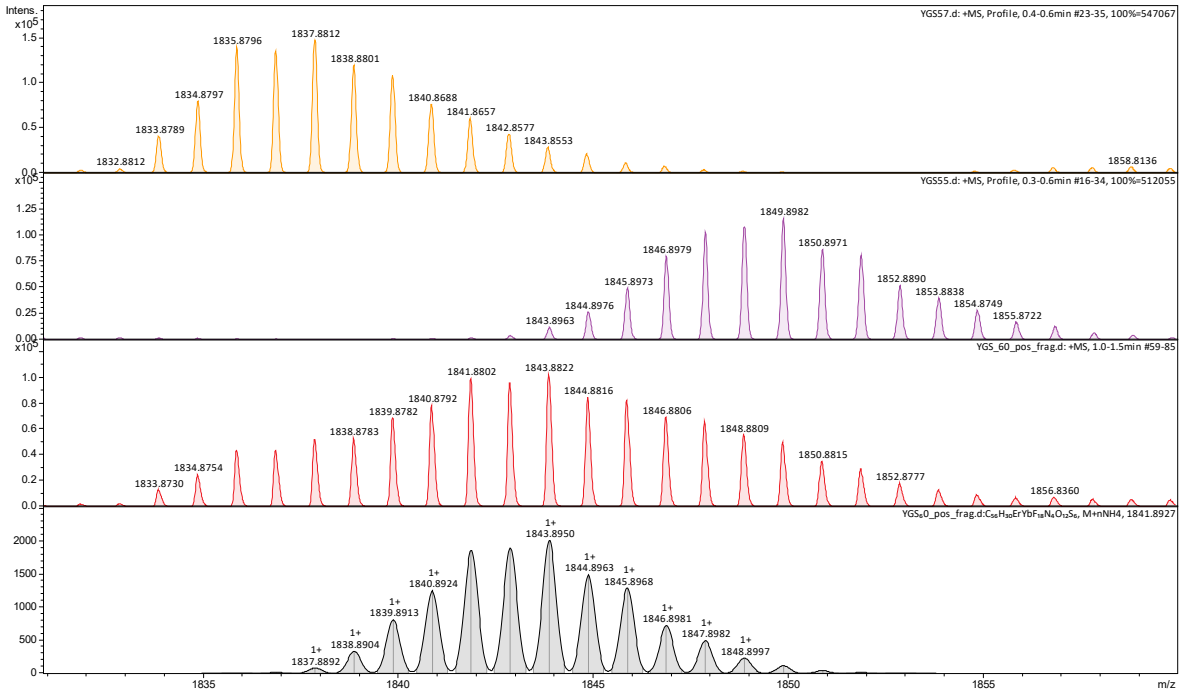

Figure S11. Comparison of the selected region of the experimental ESI-MS spectra of compound **1** (red), **2** (purple), **3** (yellow) and calculated signals corresponding to $[M+NH_4]^+$ ion (gray).

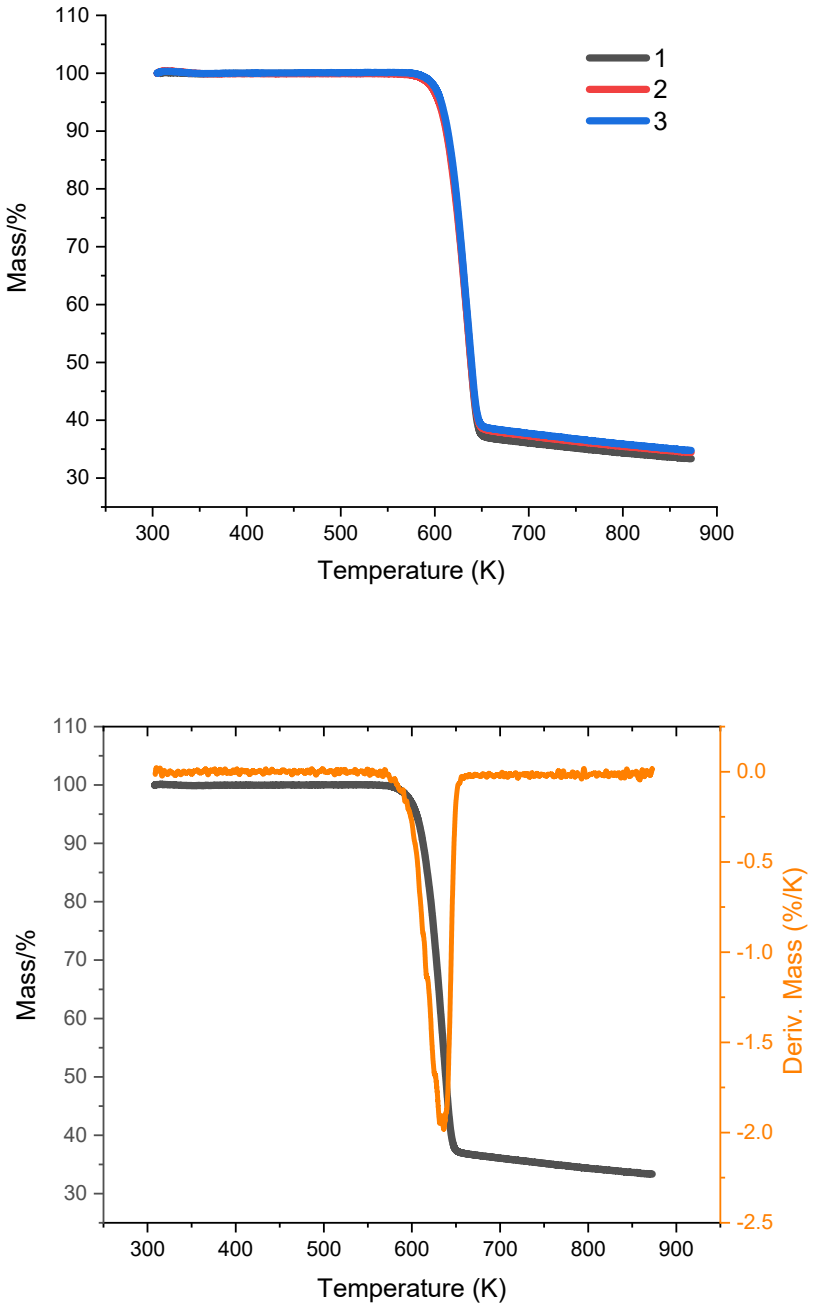

Figure S12. TGA for complexes **1-3** (top) and TGA/DTA for **1** (bottom).

3. Photoluminescence Characterization

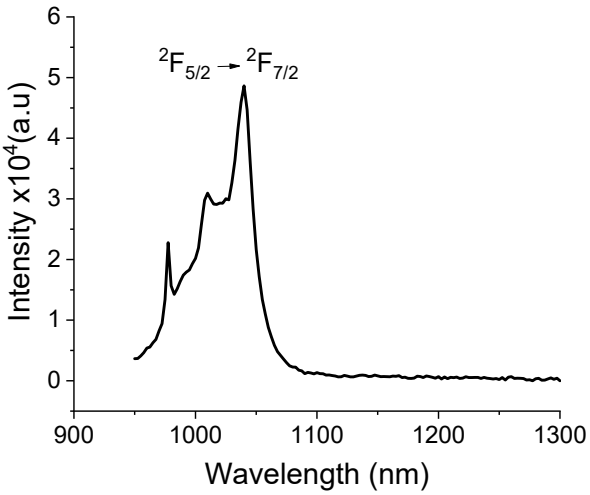

Figure S13. Near-infrared emission spectra for **2** upon 394 nm excitation at room temperature.

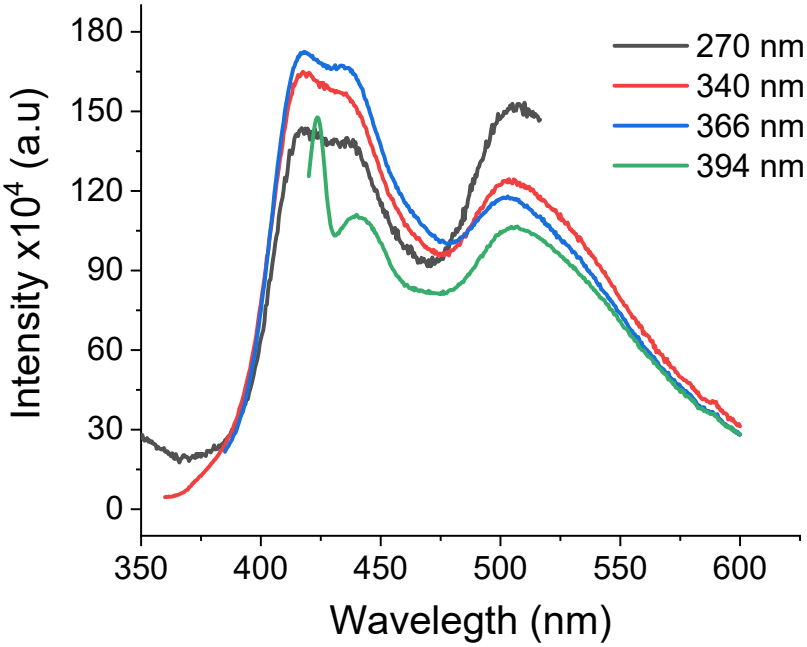

Figure S14. Solid-emission spectra of [{Gd(tta)$_3$}$_2$(μ^2-bpm)] recorded at room temperature and using different excitation wavelengths.

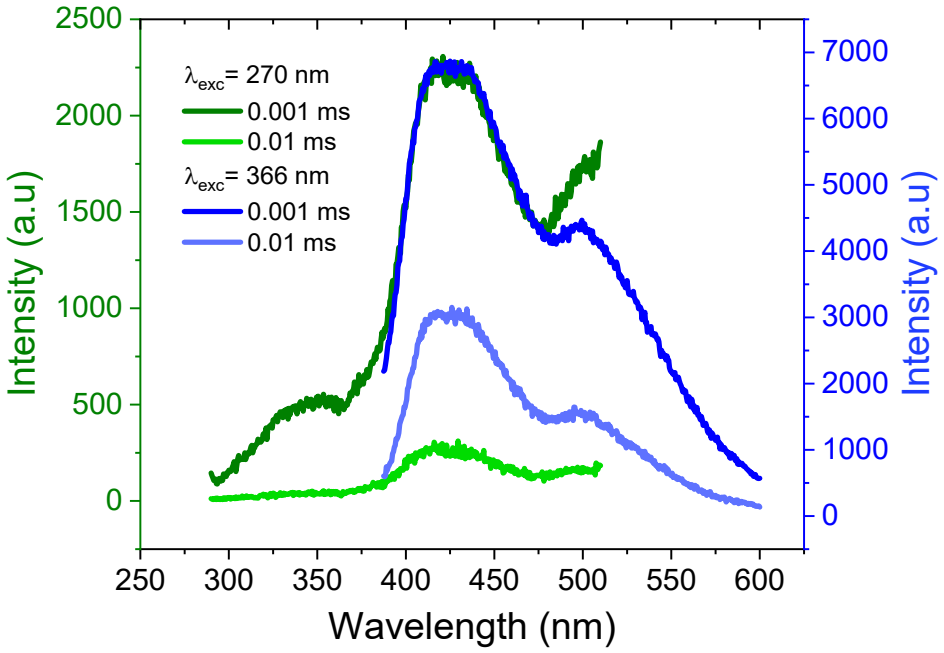

Figure S15. Phosphorescence spectra of [{Gd(tta)$_3$}$_2$(μ^2-bpm)] recorded at 270 nm (green) and 366 nm (blue) excitation at 16.5 K and P= 5.6x10^{-5} mbar and using different delay times.

4. Thermometric Characterization

The integrated areas of the Yb^{3+} ($^2F_{5/2} \rightarrow {}^2F_{7/2}$) and Er^{3+} ($^4I_{13/2} \rightarrow {}^4I_{15/2}$) bands of (**1**) were performed using MatLab® software. The uncertainties in the integrated areas of these bands ($^{\delta I_i}$) were calculated from the emission spectra evaluating the signal-to-noise ratio (SNR= signal/noise). For this, the signal fluctuations (standard deviation, considered as the noise) was determined from the emission spectra in the 1350-1400 nm range. Thus:

$$\delta I_i = \frac{1}{SNR} I_i \qquad \text{S1}$$

where i = Yb^{3+} or Er^{3+}. The uncertainty in Δ is defined as:

$$\delta\Delta = \Delta \times \sqrt{\left(\frac{\delta I_{Yb}}{I_{Yb}}\right)^2 + \left(\frac{\delta I_{Er}}{I_{Er}}\right)^2} \qquad \text{S2}$$

On the other hand, a spectral deconvolution procedure using OriginLab© software was implemented to calculate the integrated areas of the Stark splitting of Yb^{3+} ($^2F_{5/2} \rightarrow {}^2F_{7/2}$) transition for **1** and **2**. In the case of the areas of Er^{3+} ($^2H_{11/2} \rightarrow {}^4I_{15/2}$) and ($^4S_{3/2} \rightarrow {}^4I_{15/2}$) bands for **1** and **3**, were calculated from the numerical integration in the 18622-19474 cm^{-1} and 17529-18622 cm^{-1} range, respectively. First, a

baseline subtraction to remove the spectrometer electric noise was done, followed by the conversion of the signal of each emission spectrum from wavelength to energy units by applying the Jacobian transformation.[4] On the other hand, the relative uncertainty on Δ ($\delta\Delta/\Delta$) was considered as the noise-to-signal ratio (SNR) of the emission spectra resulting in a minimum $\delta\Delta/\Delta$ of 0.7%.

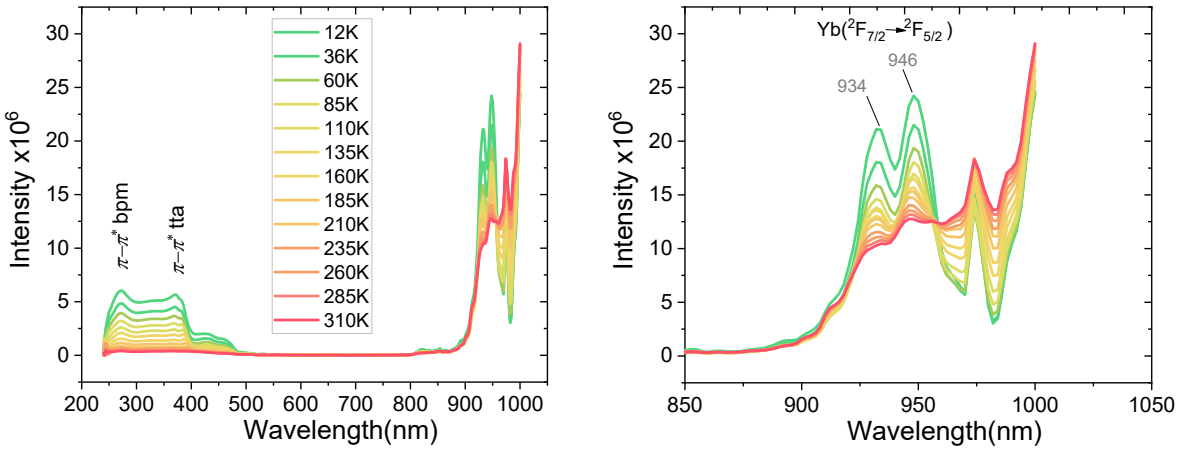

Figure S16. (Left) Excitation spectrum as function of the temperature for **1** monitoring 1040 nm emission band. (Right) Enlarged view in the range of 850-1050 nm.

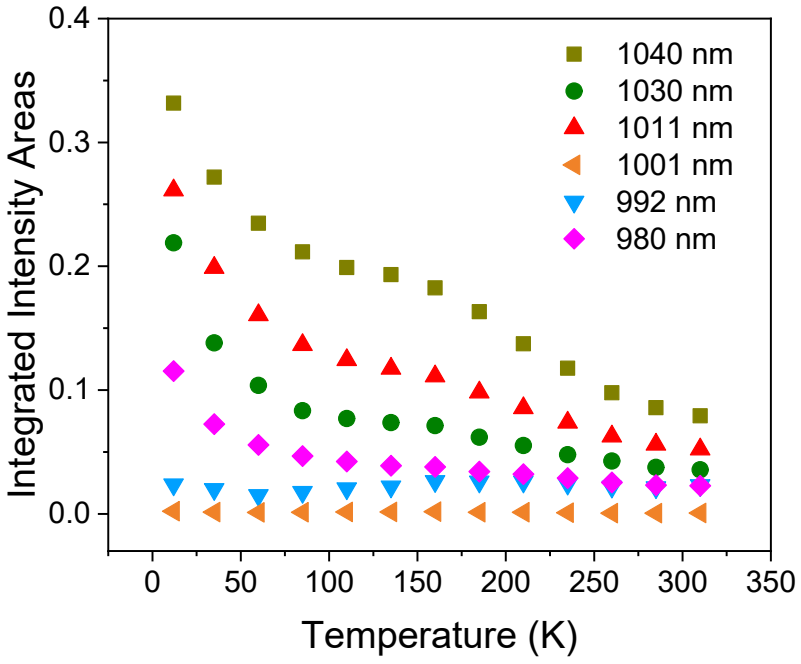

Figure S17. The temperature dependence of the integrated areas of the Stark components for the Yb^{3+} ($^2F_{5/2}\rightarrow{}^2F_{7/2}$) transition in **1**.

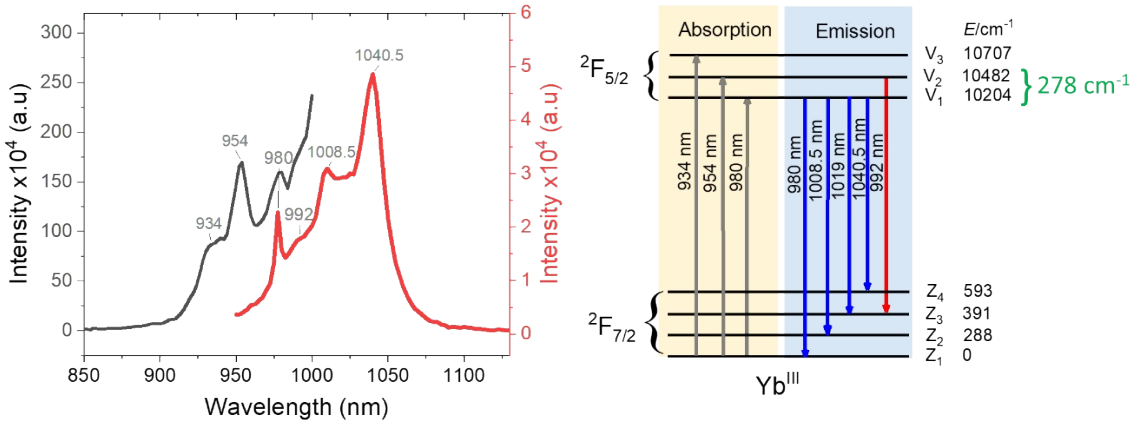

Figure S18. (Left) Solid-state excitation spectra monitoring 1040 nm emission band (black) and emission spectra upon 394 nm excitation (red) at room temperature for complex **2**. (Right) Energy level diagram for the Yb^{3+} ($^2F_{5/2} \rightarrow {}^2F_{7/2}$) transition in **2**.

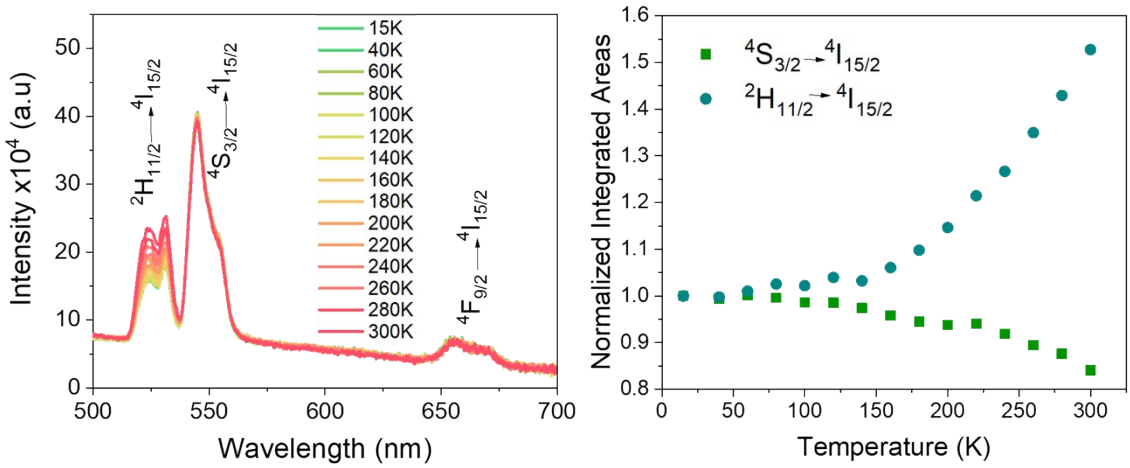

Figure S19. (Left) Solid-state visible emission spectra for **3** upon 394 nm excitation at different temperatures (from 15 to 300 K). (Right) Temperature dependence of the normalized integrated areas of the of bluish green ($^2H_{11/2} \rightarrow {}^4I_{15/2}$) and green ($^4S_{3/2} \rightarrow {}^4I_{15/2}$) bands of Er^{3+} ion in **3**.

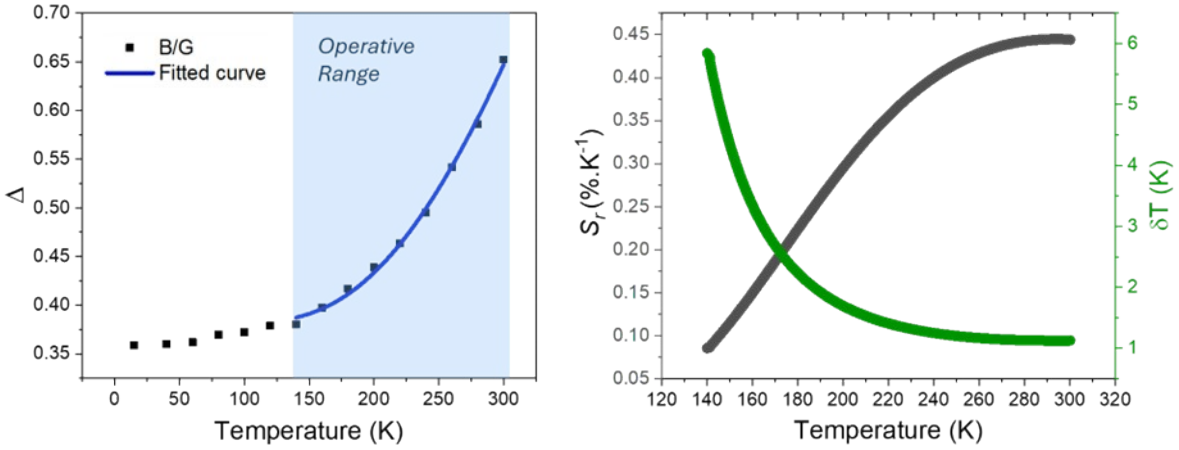

Figure S20. (Left) Temperature dependence of Δ defined as the ratio between the integrated areas of bluish green and green Er^{3+} bands for **3**, and (Right) the corresponding relative sensitivity (S_r) and temperature uncertainty (δT). The blue area depicts the operative temperature range, and the blue line represents the best fit to the experimental data (fit details in Table S7).

Table S7. Summary of the fitting parameters for the plots of complexes **1**, **2** and **3**.

Plot	Exponential	y0	A1	t1	A2	t2
Figure 4c	y = A1*exp(-x/t1) + A2*exp(-x/t2) + y0	-2.14 ± 2.28	9.86 ± 2.28	21.28 ± 7.91	8.44 ± 1.38	312.96 ± 177.21
	Linear	A	B			
Figure 5c	y = A + B*x	0.004 ± 8.32E-4	3.54E-4 ± 6.35E-6			
	Boltzmann (eq. 4)	ln(B)	$-\Delta E/k_B$			
Figure 6c	$\ln(y) = \ln(B) - \frac{\Delta E}{k_B T}$	-0.24 ± 0.02	-437.66 ± 3.97			
	Quasi-Boltzmann (eq. 6)	A	B	ΔE		
Figure 7c	y= A+B*exp(-ΔE/K_B*T)	0.41 ± 0.005	5.53 ± 0.82	626.59 ± 32.40		
Figure S20-left		0.38 ± 0.005	6.80 ± 1.36	675.71 ± 43.06		

5. Theoretical calculations

Density Functional Theory (DFT) calculations were employed to investigate the structural and electronic properties of the system, including the ground-state molecular geometry and the molecular orbital compositions of the excited singlet and triplet states involved in the energy transfer process. Geometry optimizations were performed using the Gaussian 16 software package,[5] applying the M06-L functional.[6, 7] The Def2-SVP basis set was used for hydrogen, carbon, and nitrogen atoms,[8] while the lanthanide ions (Ln^{3+} = Er^{3+} or Yb^{3+}) were treated with the MWB57 or MWB59 basis sets, respectively.[9, 10] These basis sets include effective core potentials that account for 57 or 59 core electrons, along with their corresponding valence basis sets for the lanthanide ions.

Figure S21 shows the superposition of the DFT-optimized structure (represented by pink spheres) with the crystallographic structure of complex **1**. The calculated geometry is in agreement with the experimental data, with root-mean-square deviations (RMSD) of 0.302 Å when considering only the coordination polyhedra and 1.183 Å for the entire molecule.

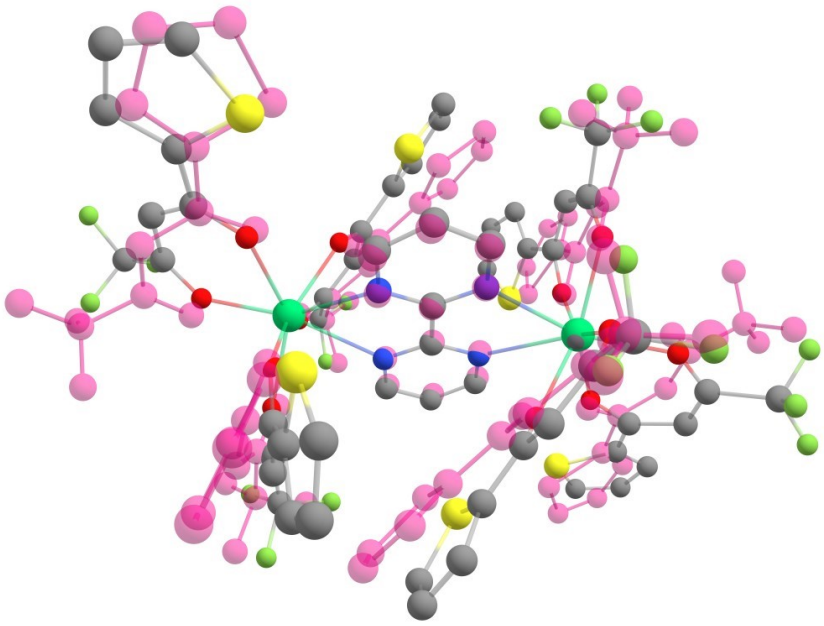

Figure S21. Superposition of the DFT-optimized structure (pink spheres) and the crystallographic structure (coloured atoms) of complex **1**. RMSD values are 0.302 Å for the coordination polyhedra and 1.183 Å for the full structure.

Time-dependent density functional theory (TD-DFT) calculations revealed distinct characteristics for the excited states involved in the energy transfer process. Notably, two triplet states were identified: a lower-energy triplet (T_1) predominantly localized on the tta ligands, and a higher-energy triplet (T_2) mainly centred on the bpm ligand. In contrast, the first excited singlet state (S_1) exhibits a more

delocalized character, with molecular orbital contributions distributed across the entire complex, without a clear preference for a specific ligand type. These spatial distributions of the occupied and unoccupied molecular orbitals associated with S_1, T_2 (bpm), and T_1 (tta) are illustrated in Figure S22.

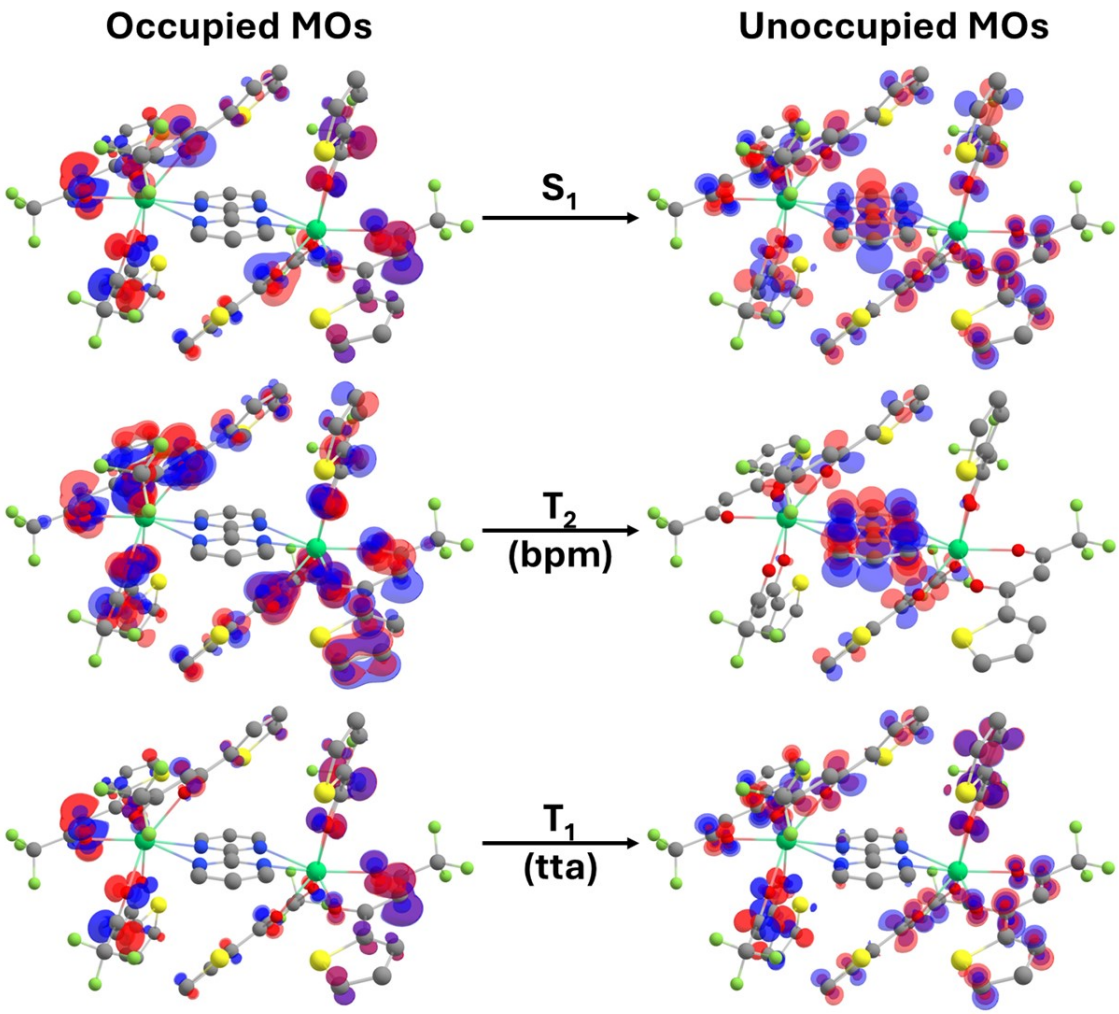

Figure S22. Molecular orbitals (MOs) involved in the S_1, T_2 (bpm), and T_1 (tta) excited states. Occupied orbitals are shown on the left and unoccupied orbitals on the right, highlighting the localization of each state. Isosurfaces generates with 0.05 e/a_0^3.

Based on the TD-DFT results, we calculated the donor–acceptor (ligand-to-Ln^{3+}) distances associated with the S_1, T_2, and T_1 states, following the methodology described in reference.[11] The individual and average values of these distances, along with the corresponding excitation energies, are summarized in Table S8.

Table S8. Ligand excited states, their calculated excitation energies, and corresponding donor–acceptor (R_L) distances. Oscillator strengths (f_{osc}) are provided for the singlet transitions and considered in the average values of energy and R_L.

State	Energy (nm)	R_L (Å)
S_1 (tta + bpm)	422.65 (f_{osc} = 0.0103)	5.75
	403.23 (f_{osc} = 0.0152)	4.46
	402.21 (f_{osc} = 0.0134)	5.82
Average	408.02	5.27
T_2 (bpm)	440.91	3.99
	439.23	4.57
	438.05	3.99
	430.61	3.99
	426.99	3.99
	422.06	4.20
	420.25	3.99
	413.53	3.99
Average	428.95	4.09
T_1 (tta)	501.40	3.84
	501.17	3.99
	496.80	3.88
	496.74	3.77
Average	499.03	3.87

Since the T_1 and T_2 states are primarily localized on different ligands (tta and bpm, respectively), it is possible to estimate the interligand energy transfer (ILET) distance based on the separation between their molecular orbital centroids (Figure S23). The shortest centroid-to-centroid distance between tta and bpm is 4.83 Å, as illustrated in Figure S23.

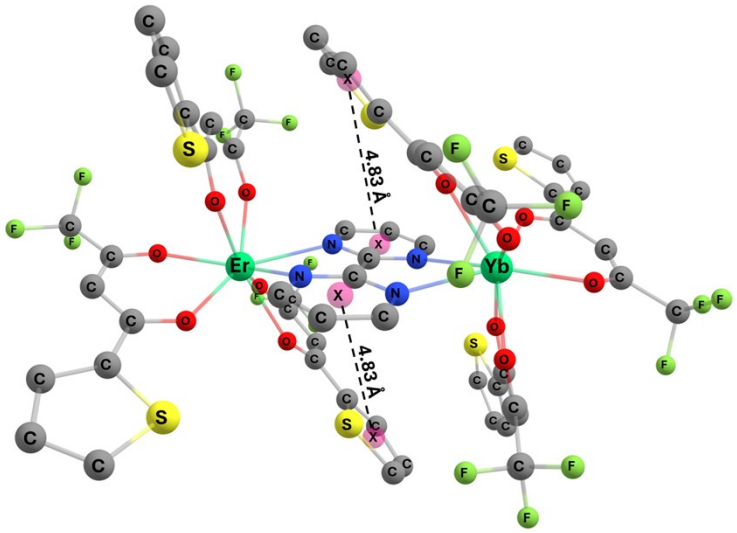

Figure S23. Optimized structure of the Er–Yb complex highlighting the shortest distance (4.83 Å) between the centroids of the tta and bpm ligands.

5.1. Energy transfer analysis

The sensitization process of [{Ln(tta)$_3$}$_2$(μ^2-bpm)] compounds involve complex and distinctive interactions. In addition to the conventional ligand-to-Ln energy transfer, interligand energy transfer also occurs. This is enabled by the near-resonance of the triplet states associated with tta and bpm, as predicted by TD-DFT calculations, and by the close energetic alignment of their centroids, which facilitates efficient tta–bpm energy transfer. Furthermore, under these conditions, a thermally activated back-transfer process can take place, whereby energy from the lower-energy triplet state T_1 (tta) is transferred to the higher-energy triplet state T_2 (bpm) as the temperature increases.

To evaluate the rates of this interligand energy transfer, we applied Förster's dipole–dipole (Eq. S3) and Dexter's exchange (Eq. S4) mechanisms, as detailed in the literature:[12, 13]

$$k_{d-d} = \frac{2\pi}{\hbar} \frac{S_D S_A}{g_D g_A R^6} \rho \qquad \text{S3}$$

Here, S_D and S_A denote the dipole strengths of the donor and acceptor electronic transitions of the ligands (T_1 and T_2, respectively), with degeneracies g_D and g_A (equal to 3 for triplet states). These dipole strengths can be estimated using the relation $S = 3\hbar/(32\pi^3\delta^3\tau)$, where δ is the barycenter of the transition and τ is the lifetime.

$$k_{ex} = \frac{2\pi e^4}{\hbar R^2} \langle \phi^* | \pi^* \rangle^2 \langle \phi | \pi \rangle^2 \rho \qquad \text{S4}$$

With $\langle \phi^* | \pi^* \rangle$ and $\langle \phi | \pi \rangle$ representing the overlap integrals between the donor (($|\pi\rangle$ and $|\pi^*\rangle$) and acceptor ($|\phi\rangle$ and $|\phi^*\rangle$) states, with values typically ranging between 0.01 and 0.10, as reported by Faustino et al.[14] Both Eq. 3 and Eq. 4 exhibit a dependence on the donor–acceptor distance R, as illustrated in Figure S23.

In addition, ρ i corresponds to the spectral overlap integral between the donor and acceptor bands, obtained from the phosphorescence spectra shown in Figures S14 and S15 for [{Gd(tta)$_3$}$_2$(μ^2-bpm)] excited at 366 nm. Two main contributions can be distinguished: the more intense peak at higher energy is attributed to the bpm moiety, while the weaker, lower-energy peak arises from the tta ligand. These assignments are consistent with the TD-DFT results (Figure S22 and Table S8).

The phosphorescence spectrum was converted from wavelength to wavenumber using a Jacobian transformation[4] and subsequently deconvoluted into Gaussian functions, revealing a clear spectral overlap between bpm and tta (Figure S24a).

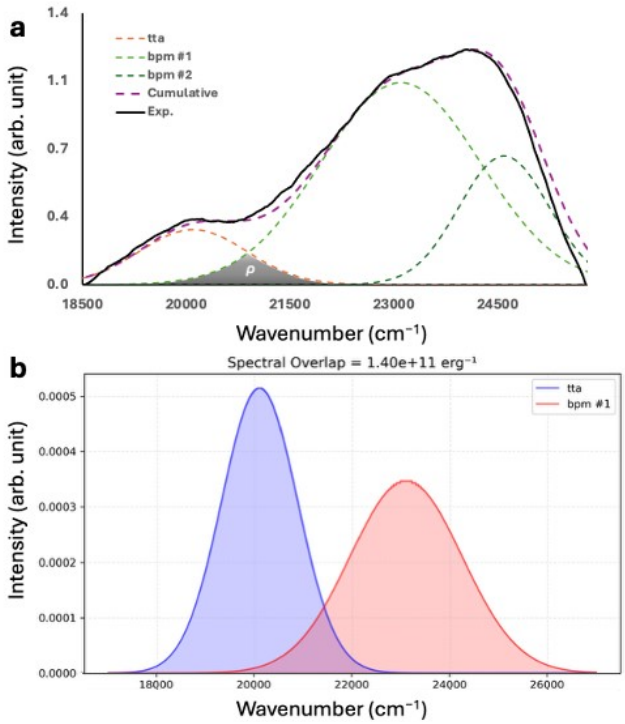

Figure S24. Spectral treatment of the phosphorescence band. (a) Jacobian transformation of the experimental spectrum (black line) and Gaussian function fittings (dashed lines) corresponding to tta (orange) and bpm (light green and dark green). The cumulative profile, obtained as the sum of these three Gaussian functions, closely reproduces the experimental phosphorescence band. The spectral overlap ρ is highlighted as the grey-filled area. b) Calculated spectral overlap ($\rho = 1.40 \times 10^{11}$ erg^{-1}) between the tta and bpm triplet states.

The value of ρ can be obtained by integrating the product of the normalized Gaussian functions representing the donor and acceptor spectral bands:

$$\rho = \int_0^\infty G_D G_A dE \qquad \text{S5}$$

Here, G_D and G_A represent the Gaussian functions for the donor and acceptor bands, respectively. Each Gaussian function is defined by:

$$G(E) = \frac{1}{\sigma\sqrt{\pi/2}} e^{-2\left(\frac{E-E_0}{\sigma}\right)^2} \qquad \text{S6}$$

Where σ is the bandwidth and E_0 is the energy of the maximum intensity of the curve. For the curves shown in Figure S24b, $\sigma = 1550$ and 2300 cm^{-1}, and $E_0 = 20100$ and 23100 for the tta (donor) and bpm (acceptor), respectively. Using these values, the spectral overlap integral ρ is 2.77×10^{-5} cm. To convert to the common units of erg^{-1}, this value is divided by 1.986 ×10^{-16} erg^{-1}/cm, resulting in a final value of $\rho = 1.40 \times 10^{11}$ erg^{-1}.

Supporting Information

The backward energy transfer from tta → bpm i is estimated by applying a Boltzmann factor to the forward energy transfer process (bpm → tta), as described by Eqs. S3 and S4.

We now analyze the sensitization process from the ligands (tta and bpm) to the lanthanide ions (Yb^{3+} and Er^{3+}), commonly referred to as the antenna effect. The energy transfer rates from the ligands to the Ln^{3+} ions can be determined following the procedures described in references.[15, 16]

Specifically, the rates associated with the dipole–dipole (W_{d-d}, Eq. S7), dipole-multipole (W_{d-m}, Eq. S8), and exchange (W_{ex}, Eq. S9) mechanisms are calculated as follows:

$$W_{d-d} = \frac{S_L (1-\sigma_1)^2 4\pi e^2}{(2J+1) g \hbar R_L^6} \sum_{\lambda} \Omega_{\lambda}^{FED} \left| \langle \psi' J' \| U^{(\lambda)} \| \psi J \rangle \right|^2 F \quad \text{S7}$$

$$W_{d-m} = \frac{S_L}{(2J+1) g} \frac{2\pi e^2}{\hbar} \sum_{\lambda} (\lambda+1) \frac{\langle r^{\lambda} \rangle^2}{\left(R_L^{\lambda+2}\right)^2} \langle f \| C^{(\lambda)} \| f \rangle^2 \times (1-\sigma_{\lambda})^2 \left| \langle \psi' J' \| U^{(\lambda)} \| \psi J \rangle \right|^2 F \quad \text{S8}$$

$$W_{ex} = \frac{(1-\sigma_0)^2 8\pi e^2}{(2J+1) G \hbar R_L^4} \left| \langle \psi' J' \| S \| \psi J \rangle \right|^2 \sum_{m} \left| \left\langle \phi \left| \sum_{j} \mu_z(j) s_m(j) \right| \phi^* \right\rangle \right|^2 F \quad \text{S9}$$

where R_L denotes the distance between the lanthanide ion and the region of the ligand where the donor (or acceptor) electronic state is primarily localized. This region typically corresponds to aromatic rings and unsaturated bonds, as observed in phenylsulfonyl amidophosphate-based ligands[17] and ancillary ligands such as bipyridine.[18] The specific values of R_L for the dinuclear complex under study are reported in Table S8.

In Eq. S7, Ω_{λ}^{FED} represents the intensity parameters that only consider the forced electric dipole mechanism (FED). In this study, these parameters were calculated using a charge factor of 1 within the Simple Overlap Model (SOM) for the ligand field.[19, 20]

The $\left| \langle \psi' J' \| U^{(\lambda)} \| \psi J \rangle \right|^2$ are squared reduced matrix elements of the tensor operator of rank λ for the $|\psi' J'\rangle \longrightarrow |\psi J\rangle$ transition and their values are tabulated in[21] for Er^{3+} transitions and in[22] for the Yb^{3+} $^2F_{7/2} \rightarrow {}^2F_{5/2}$ transition. The $\left\langle 4f^{13}, {}^2F_{5/2} \middle| |S| \middle| 4f^{13}, {}^2F_{7/2} \right\rangle^2 = 3.429$ matrix element is non-zero for the case of Yb^{3+} $^2F_{7/2} \rightarrow {}^2F_{5/2}$ transition[23] while almost all transitions involving the ground state of the Er^{3+} are zero ($\Delta J \neq 0, \pm 1$). S_L is the dipole strength of the ligand transition (donor), $\langle r^{\lambda} \rangle$ are the $4f$ radial integrals, g is the ligand state degeneracy (1 for S_1 and 3 for T_1 and T_2), $\langle f \| C^{(\lambda)} \| f \rangle$ is the reduced matrix element of Racah's tensor operators, and $(1-\sigma_{\lambda})$ are the shielding factors for electric multipolar interactions while $(1-\sigma_0)$ is the shielding factor for the electric monopole.[16, 24-26]

In Eq. S9, ^{S}m is the spin operator in the ligand, μ_z is the dipole operator (its z-component) and it assumes values of ~10^{-36} (e.s.u.).[16, 27]

In the above equations, J represents the total angular momentum quantum number of the lanthanide ion, specifying its 4f spectroscopic term. The term F appearing in Eqs. S7–S9 is the spectral overlap factor for the ligand-Ln^{3+} transitions, which accounts for the energy mismatch condition between the donor and acceptor states. For ligand-to-Ln energy transfer, an analytical expression for F can be employed:

$$F = \frac{1}{\hbar\sigma_L}\sqrt{\frac{ln(2)}{\pi}}e^{-\left(\frac{\Delta}{\hbar\sigma_L}\right)^2 ln(2)} G(\Delta,T) \quad \text{S10}$$

where Δ is the energy difference between donor state (D) and lanthanide ion acceptor state ($\Delta = E_D - E_{Ln}$) and σ_L is the bandwidth of the ligand state.[16, 28] The function $G(\Delta,T)$ is the energy barrier factor given by $\exp\left(\Delta/k_BT\right)$, with k_B and T being the Boltzmann constant and temperature. This is activated only when the energy transfer pathway has negative values Δ, otherwise, $G(\Delta,T) = 1$.

The energy transfer rates of a pathway $W(p)$ are determined by summing all the mechanisms within that pathway (p):

$$W(p) = W_{d-d}(p) + W_{d-m}(p) + W_{ex}(p) \quad \text{S11}$$

The energy transfer rates from S_1 (W^S), T_1 (W^{T1}), and T_2 (W^{T2}), and their corresponding backward rates (W_b^S, W_b^T, and W_b^{T2}, respectively) are calculated by summing over all individual pathways:

$$W_a^C = \sum_p W(C,a,p) \quad \text{S12}$$

In this context, the superscript C stands for either S (representing the IET rate involving the S_1 state) or T (involving T_1 and T_2 states) channels, while the subscript a represents the direction of the energy transfer flow. The absence of a letter in the subscript represents forward transfer (*i.e.*, ligand-to-lanthanide energy transfer), and when the letter b appears, it indicates backward transfer (*i.e.*, lanthanide-to-ligand energy transfer).

Tables S8-S11 present the calculated energy transfer pathways and their associated rates involving the tta and bpm ligands transferring energy to the Er^{3+} and Yb^{3+} ions. For energy transfer to the Er^{3+} ion, the exchange mechanism is only allowed in pathways 1 and 13 due to the selection rule $\Delta J = 0, \pm 1$. However, because of non-resonant conditions (large $|\Delta|$ values), he exchange mechanism can be neglected. The dipole–multipole mechanism dominates, particularly in pathway 6 of the forward energy transfer (i.e., tta [$T_1 \rightarrow S_0$] → Er^{3+} [$^4I_{15/2} \rightarrow {}^2H_{11/2}$] and bpm [$T_1 \rightarrow S_0$] → Er^{3+} [$^4I_{15/2} \rightarrow {}^2H_{11/2}$]), contributing approximately 99.9% and 99.3% of the total transfer rate, respectively.

In contrast, the back energy transfer involving Er^{3+} shows a different behaviour due to varying resonance conditions for tta (Table S9) and bpm (Table S10). The tta receives contributions from two pathways: Er^{3+} [$^2H_{11/2}\rightarrow{}^4I_{15/2}$] → tta [$S_0\rightarrow T_1$] and Er^{3+} [$^4F_{7/2}\rightarrow{}^4I_{15/2}$] → tta [$S_0\rightarrow T_1$] (pathway 21 and 22, Table S9). Conversely, bpm has only one significant contribution from a higher energy transition, Er^{3+}[$^4G_{11/2}\rightarrow{}^4I_{15/2}$] → bpm [$S_0\rightarrow T_1$] (pathway 26, Table S10), which is also the highest rate calculated for the Er^{3+} ion (1.8×10^5 s^{-1}).

For the Yb^{3+} ion, the $^2F_{7/2}\rightarrow{}^2F_{5/2}$ transition is strongly influenced by the exchange mechanism despite the large energy gap between the tta triplet state and the Yb^{3+} transition (Δ = 9860 cm^{-1}). This influence is compensated by the large value of the reduced spin matrix elements $\left\langle 4f^{13},{}^2F_{5/2}\right|\left|S\right|\left|4f^{13},{}^2F_{7/2}\right\rangle^2 = 3.429$, as discussed in detail in Ref.[23]

In summary, as the temperature increases, the tta ligand loses population to the bpm ligand through interligand energy transfer. Subsequently, bpm transfers energy to the Er^{3+} ion, particularly to the $^2H_{11/2}$ level from where the $^2H_{11/2}\rightarrow{}^4I_{15/2}$ band is originated. From this level, non-radiative decay through lower 4f states populate the $^4S_{3/2}$ and $^4F_{9/2}$ levels, giving rise to the corresponding $^4S_{3/2}\rightarrow{}^4I_{15/2}$ and $^4F_{9/2}\rightarrow{}^4I_{15/2}$ emission bands. Conversely, at low temperatures, the population of the Yb^{3+} $^2F_{5/2}$ state is higher because the tta → bpm energy transfer is not activated, making the direct tta → Yb^{3+} energy transfer more efficient

Table S9. Calculated forward tta-to-Er^{3+} and backward Er^{3+}-to-tta energy transfer rates at 300 K.

p	Donor	Acceptor	Contr. (%)	Δ (cm^{-1})	W (s^{-1})	W_{d-d} (s^{-1})	W_{d-m} (s^{-1})
1	$T_1\rightarrow S_0$	$^4I_{15/2}\rightarrow{}^4I_{13/2}$	0.0	13605	1.0E-20	1.0E-21	8.9E-21
2	$T_1\rightarrow S_0$	$^4I_{15/2}\rightarrow{}^4I_{11/2}$	0.0	9971	7.0E-10	1.5E-11	6.9E-10
3	$T_1\rightarrow S_0$	$^4I_{15/2}\rightarrow{}^4I_{9/2}$	0.0	7720	5.2E-07	3.7E-07	1.5E-07
4	$T_1\rightarrow S_0$	$^4I_{15/2}\rightarrow{}^4F_{9/2}$	0.0	4862	1.1E-01	9.3E-02	1.7E-02
5	$T_1\rightarrow S_0$	$^4I_{15/2}\rightarrow{}^4S_{3/2}$	0.0	1734	1.0E+01	1.0E+01	5.7E-03
6	$T_1\rightarrow S_0$	$^4I_{15/2}\rightarrow{}^2H_{11/2}$	99.9	980	3.9E+04	4.2E+01	3.9E+04
7	$T_1\rightarrow S_0$	$^4I_{15/2}\rightarrow{}^4F_{7/2}$	0.0	-398	1.2E+01	1.1E+01	5.8E-01
8	$T_1\rightarrow S_0$	$^4I_{15/2}\rightarrow{}^4F_{5/2}$	0.0	-2059	3.6E-04	3.6E-04	2.0E-07
9	$T_1\rightarrow S_0$	$^4I_{15/2}\rightarrow{}^4F_{3/2}$	0.0	-2395	2.7E-05	2.7E-05	1.5E-08
10	$T_1\rightarrow S_0$	$^4I_{15/2}\rightarrow{}^4H_{9/2}$	0.0	-4439	4.9E-11	4.8E-11	1.3E-12
11	$T_1\rightarrow S_0$	$^4I_{15/2}\rightarrow{}^4G_{11/2}$	0.0	-6314	4.7E-14	5.1E-17	4.7E-14
12	$T_1\rightarrow S_0$	$^4I_{15/2}\rightarrow{}^4G_{9/2}$	0.0	-7320	4.0E-21	3.3E-21	7.1E-22
13	$T_1\rightarrow S_0$	$^4I_{15/2}\rightarrow{}^2K_{15/2}$	0.0	-7605	1.2E-20	7.2E-23	1.2E-20
14	$T_1\rightarrow S_0$	$^4I_{15/2}\rightarrow{}^4G_{7/2}$	0.0	-7907	7.2E-24	6.9E-24	2.8E-25
15	$T_1\rightarrow S_0$	$^4I_{15/2}\rightarrow{}^2P_{1/2}$	0.0	-13002	0.0E+00	0.0E+00	0.0E+00
				W^{T1}	3.9E+04		
16	$^4I_{13/2}\rightarrow{}^4I_{15/2}$	$S_0\rightarrow T_1$	0.0	-13605	5.3E-49	5.6E-50	4.7E-49
17	$^4I_{11/2}\rightarrow{}^4I_{15/2}$	$S_0\rightarrow T_1$	0.0	-9971	1.6E-30	3.5E-32	1.6E-30

18	$^4I_{9/2}\rightarrow{}^4I_{15/2}$	$S_0\rightarrow T_1$	0.0	-7720	7.2E-23	5.2E-23	2.1E-23
19	$^4F_{9/2}\rightarrow{}^4I_{15/2}$	$S_0\rightarrow T_1$	0.0	-4862	1.4E-11	1.2E-11	2.1E-12
20	$^4S_{3/2}\rightarrow{}^4I_{15/2}$	$S_0\rightarrow T_1$	0.0	-1734	1.2E-02	1.2E-02	6.9E-06
21	$^2H_{11/2}\rightarrow{}^4I_{15/2}$	$S_0\rightarrow T_1$	70.4	-980	4.8E+02	5.2E-01	4.8E+02
22	$^4F_{7/2}\rightarrow{}^4I_{15/2}$	$S_0\rightarrow T_1$	24.4	398	1.7E+02	1.6E+02	8.4E+00
23	$^4F_{5/2}\rightarrow{}^4I_{15/2}$	$S_0\rightarrow T_1$	3.1	2059	2.1E+01	2.1E+01	1.2E-02
24	$^4F_{3/2}\rightarrow{}^4I_{15/2}$	$S_0\rightarrow T_1$	1.9	2395	1.3E+01	1.3E+01	7.3E-03
25	$^4H_{9/2}\rightarrow{}^4I_{15/2}$	$S_0\rightarrow T_1$	0.0	4439	1.4E-01	1.4E-01	3.9E-03
26	$^4G_{11/2}\rightarrow{}^4I_{15/2}$	$S_0\rightarrow T_1$	0.1	6314	9.0E-01	9.8E-04	9.0E-01
27	$^4G_{9/2}\rightarrow{}^4I_{15/2}$	$S_0\rightarrow T_1$	0.0	7320	1.2E-05	9.6E-06	2.1E-06
28	$^2K_{15/2}\rightarrow{}^4I_{15/2}$	$S_0\rightarrow T_1$	0.0	7605	8.6E-05	5.0E-07	8.6E-05
29	$^4G_{7/2}\rightarrow{}^4I_{15/2}$	$S_0\rightarrow T_1$	0.0	7907	4.6E-07	4.4E-07	1.8E-08
30	$^2P_{1/2}\rightarrow{}^4I_{15/2}$	$S_0\rightarrow T_1$	0.0	13002	0.0E+00	0.0E+00	0.0E+00
				W_b^{T1}	6.8E+02		

Table S10. Calculated forward bpm-to-Er^{3+} and backward Er^{3+}-to-bpm energy transfer rates at 300 K.

p	**Donor**	**Acceptor**	**Contr. (%)**	**Δ (cm^{-1})**	W **(s^{-1})**	W_{d-d} **(s^{-1})**	W_{d-m} **(s^{-1})**
1	$T_2\rightarrow S_0$	$^4I_{15/2}\rightarrow{}^4I_{13/2}$	0.0	16605	2.6E-12	1.5E-13	2.5E-12
2	$T_2\rightarrow S_0$	$^4I_{15/2}\rightarrow{}^4I_{11/2}$	0.0	12971	4.6E-06	5.3E-08	4.6E-06
3	$T_2\rightarrow S_0$	$^4I_{15/2}\rightarrow{}^4I_{9/2}$	0.0	10720	5.4E-05	1.4E-05	4.0E-05
4	$T_2\rightarrow S_0$	$^4I_{15/2}\rightarrow{}^4F_{9/2}$	0.0	7862	2.6E-01	1.2E-01	1.5E-01
5	$T_2\rightarrow S_0$	$^4I_{15/2}\rightarrow{}^4S_{3/2}$	0.0	4734	5.9E+00	5.9E+00	8.0E-02
6	$T_2\rightarrow S_0$	$^4I_{15/2}\rightarrow{}^2H_{11/2}$	99.3	3980	5.6E+04	3.2E+01	5.6E+04
7	$T_2\rightarrow S_0$	$^4I_{15/2}\rightarrow{}^4F_{7/2}$	0.4	2602	2.0E+02	1.5E+02	5.4E+01
8	$T_2\rightarrow S_0$	$^4I_{15/2}\rightarrow{}^4F_{5/2}$	0.2	941	1.0E+02	9.8E+01	1.3E+00
9	$T_2\rightarrow S_0$	$^4I_{15/2}\rightarrow{}^4F_{3/2}$	0.1	605	6.0E+01	5.9E+01	8.1E-01
10	$T_2\rightarrow S_0$	$^4I_{15/2}\rightarrow{}^4H_{9/2}$	0.0	-1439	1.0E-01	8.7E-02	1.7E-02
11	$T_2\rightarrow S_0$	$^4I_{15/2}\rightarrow{}^4G_{11/2}$	0.0	-3314	1.7E-02	9.6E-06	1.7E-02
12	$T_2\rightarrow S_0$	$^4I_{15/2}\rightarrow{}^4G_{9/2}$	0.0	-4320	3.0E-08	1.2E-08	1.8E-08
13	$T_2\rightarrow S_0$	$^4I_{15/2}\rightarrow{}^2K_{15/2}$	0.0	-4605	2.1E-07	6.4E-10	2.1E-07
14	$T_2\rightarrow S_0$	$^4I_{15/2}\rightarrow{}^4G_{7/2}$	0.0	-4907	2.1E-10	1.6E-10	4.6E-11
15	$T_2\rightarrow S_0$	$^4I_{15/2}\rightarrow{}^2P_{1/2}$	0.0	-10002	0.0E+00	0.0E+00	0.0E+00
				W^{T2}	5.6E+04		
16	$^4I_{13/2}\rightarrow{}^4I_{15/2}$	$S_0\rightarrow T_2$	0.0	-16605	7.9E-47	4.6E-48	7.4E-47
17	$^4I_{11/2}\rightarrow{}^4I_{15/2}$	$S_0\rightarrow T_2$	0.0	-12971	6.0E-33	7.0E-35	6.0E-33
18	$^4I_{9/2}\rightarrow{}^4I_{15/2}$	$S_0\rightarrow T_2$	0.0	-10720	4.2E-27	1.1E-27	3.1E-27
19	$^4F_{9/2}\rightarrow{}^4I_{15/2}$	$S_0\rightarrow T_2$	0.0	-7862	1.9E-17	8.3E-18	1.0E-17
20	$^4S_{3/2}\rightarrow{}^4I_{15/2}$	$S_0\rightarrow T_2$	0.0	-4734	4.1E-09	4.0E-09	5.5E-11
21	$^2H_{11/2}\rightarrow{}^4I_{15/2}$	$S_0\rightarrow T_2$	0.0	-3980	3.9E-04	2.2E-07	3.9E-04
22	$^4F_{7/2}\rightarrow{}^4I_{15/2}$	$S_0\rightarrow T_2$	0.0	-2602	1.6E-03	1.2E-03	4.4E-04
23	$^4F_{5/2}\rightarrow{}^4I_{15/2}$	$S_0\rightarrow T_2$	0.0	-941	3.3E+00	3.2E+00	4.4E-02

24	$^4F_{3/2}\rightarrow{}^4I_{15/2}$	$S_0\rightarrow T_2$	0.0	-605	1.7E+01	1.6E+01	2.2E-01
25	$^4H_{9/2}\rightarrow{}^4I_{15/2}$	$S_0\rightarrow T_2$	0.1	1439	1.7E+02	1.4E+02	2.9E+01
26	$^4G_{11/2}\rightarrow{}^4I_{15/2}$	$S_0\rightarrow T_2$	99.4	3314	1.8E+05	1.1E+02	1.8E+05
27	$^4G_{9/2}\rightarrow{}^4I_{15/2}$	$S_0\rightarrow T_2$	0.0	4320	4.9E+01	2.0E+01	2.9E+01
28	$^2K_{15/2}\rightarrow{}^4I_{15/2}$	$S_0\rightarrow T_2$	0.4	4605	8.2E+02	2.5E+00	8.2E+02
29	$^4G_{7/2}\rightarrow{}^4I_{15/2}$	$S_0\rightarrow T_2$	0.0	4907	7.5E+00	5.8E+00	1.7E+00
30	$^2P_{1/2}\rightarrow{}^4I_{15/2}$	$S_0\rightarrow T_2$	0.0	10002	0.0E+00	0.0E+00	0.0E+00
				W_b^{T2}	1.8E+05		

Table S11. Calculated forward tta-to-Yb^{3+} and backward Yb^{3+}-to-tta energy transfer rates at 300 K.

p	**Donor**	**Acceptor**	**Δ (cm⁻¹)**	W **(s⁻¹)**	W_{d-d} **(s⁻¹)**	W_{d-m} **(s⁻¹)**	W_{ex}
1	$T_1\rightarrow S_0$	$^2F_{7/2}\rightarrow{}^2F_{5/2}$	9860	2.2E+06	4.2E-02	8.0E+00	2.2E+06
2	$^2F_{5/2}\rightarrow{}^2F_{7/2}$	$S_0\rightarrow T_1$	-9860	9.0E-15	1.7E-22	3.2E-20	9.0E-15

Table S12. Calculated forward bpm-to-Yb^{3+} and backward Yb^{3+}-to-bpm energy transfer rates at 300 K.

p	**Donor**	**Acceptor**	**Δ (cm⁻¹)**	W **(s⁻¹)**	W_{d-d} **(s⁻¹)**	W_{d-m} **(s⁻¹)**	W_{ex}
1	$T_2\rightarrow S_0$	$^2F_{7/2}\rightarrow{}^2F_{5/2}$	12860	1.6E+01	4.1E-07	7.0E-05	1.6E+01
2	$^2F_{5/2}\rightarrow{}^2F_{7/2}$	$S_0\rightarrow T_2$	-12860	3.8E-26	9.5E-34	1.6E-31	3.8E-26

The energy transfer rates from the ligand states to the Ln^{3+} ions as a function of temperature are illustrated in Figures S25 and S26.

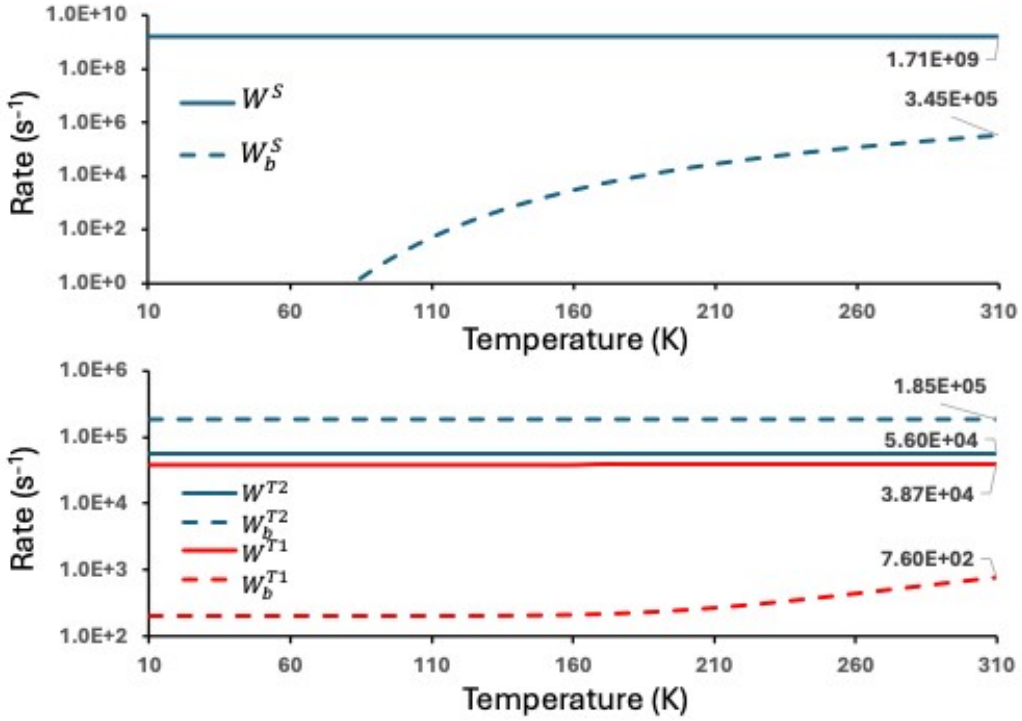

Figure S25. Energy transfer rates as a function of temperature involving the S_1, T_1, and T_2 states to the Er^{3+} ion.

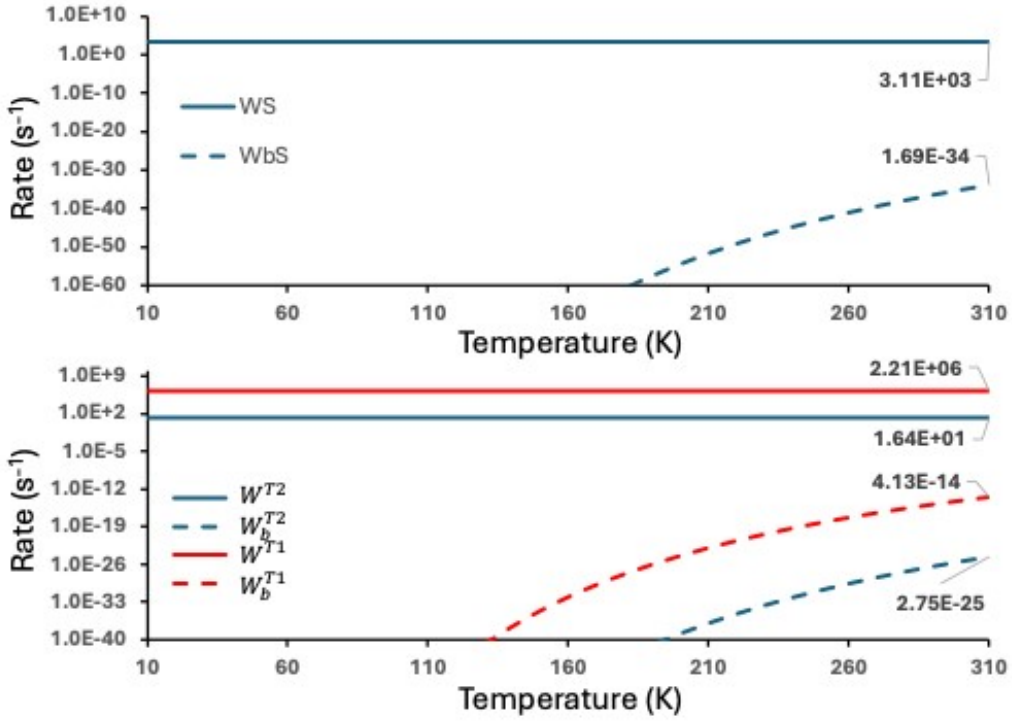

Figure S26. Energy transfer rates as a function of temperature involving the S_1, T_1, and T_2 states to the Yb^{3+} ion.

The energy transfer rates between the Yb^{3+} and Er^{3+} centers in **1** were calculated considering the dipole-dipole, dipole-quadrupole (quadrupole-dipole), quadrupole-quadrupole, and exchange mechanisms as follows:[29]

$$W_{d-d} = \frac{4\pi S_d^D S_d^A}{3\hbar \ R^6} F \qquad \text{S13}$$

$$W_{d-q} = \frac{\pi\left(S_d^D S_q^A + S_q^D S_d^A\right)}{\hbar \qquad R^8} F \qquad \text{S14}$$

$$W_{q-q} = \frac{28\pi S_q^D S_q^A}{5\hbar \ R^{10}} F \qquad \text{S15}$$

$$W_{ex} = \frac{2\pi}{\hbar}\left[\left(\frac{e^2}{R}\right)\rho_{f-f}^{\ 2}\right]^2 F \qquad \text{S16}$$

where S_d and S_q are the electric dipole and quadrupole strengths for the transitions involved – the superscript indicates if it is from the donor (D, Yb^{3+}) or acceptor (A, Er^{3+}). R is the distance between the Yb–Er centers in **1**, which is, from the crystallographic sctructure $R = 6.77$ Å. F is the spectral overlap between the donor and acceptor transitions, which contains the energy mismatch conditions (Δ) and ρ_{f-f} is the Er^{3+} $4f^{11}$ and Yb^{3+} $4f^{13}$ overlap integral.[25]

Table S13. Calculated Yb–Er energy transfer rates. W (s^{-1}) is the sum of all mechanisms with the application of the Boltzmann factor if Δ is negative. The donor transition is the Yb^{3+} $^2F_{5/2}\rightarrow{}^2F_{7/2}$.

p	Acceptor	Contr. (%)	Δ (cm^{-1})	W (s^{-1})	W_{d-d} (s^{-1})	W_{d-q}	W_{q-q} (s^{-1})	W_{ex} (s^{-1})
1	$^4I_{15/2}\rightarrow{}^4I_{13/2}$	0.0	3755	9.7E-10	2.5E-11	1.6E-10	7.8E-10	1.0E-21
2	$^4I_{15/2}\rightarrow{}^4I_{11/2}$	89.0	121	6.7E+05	4.4E+02	1.7E+04	6.5E+05	1.8E-08
3	$^4I_{15/2}\rightarrow{}^4I_{9/2}$	0.0	-2130	6.6E-07	2.6E-03	1.5E-02	0.0E+00	1.0E-12
4	$^4I_{15/2}\rightarrow{}^4F_{9/2}$	0.0	-4988	3.3E-31	1.2E-21	6.9E-21	0.0E+00	7.3E-32
5	$^4I_{15/2}\rightarrow{}^4S_{3/2}$	0.0	-8116	~0	7.0E-61	4.2E-60	0.0E+00	2.0E-70
6	$^4I_{15/2}\rightarrow{}^2H_{11/2}$	0.0	-8870	~0	3.4E-72	1.4E-70	5.1E-69	1.8E-82
7	$^4I_{15/2}\rightarrow{}^4F_{7/2}$	0.0	-10248	~0	3.6E-97	2.1E-96	0.0E+00	3.0E-107
8	$^4I_{15/2}\rightarrow{}^4F_{5/2}$	0.0	-11909	~0	2.5E-132	1.5E-131	0.0E+00	7.1E-142
9	$^4I_{15/2}\rightarrow{}^4F_{3/2}$	0.0	-12245	~0	3.2E-140	1.9E-139	0.0E+00	1.6E-149
10	$^4I_{15/2}\rightarrow{}^2H_{9/2}$	0.0	-14289	~0	5.9E-191	3.5E-190	0.0E+00	1.6E-200
11	$^4I_{15/2}\rightarrow{}^4G_{11/2}$	0.0	-16164	~0	7.4E-244	2.9E-242	1.1E-240	3.0E-254
12	$^4I_{15/2}\rightarrow{}^4G_{9/2}$	0.0	-17170	0	5.0E-276	3.0E-275	0.0E+00	8.6E-286
13	$^4I_{13/2}\rightarrow{}^4I_{11/2}$	0.0	6616	2.1E-37	2.9E-39	2.1E-38	1.9E-37	1.2E-49
14	$^4I_{13/2}\rightarrow{}^4I_{9/2}$	0.0	4365	2.3E-15	2.8E-16	1.7E-15	3.0E-16	2.2E-26
15	$^4I_{13/2}\rightarrow{}^4F_{9/2}$	0.0	1507	7.2E+01	6.0E-01	5.1E+00	6.7E+01	1.4E-10
16	$^4I_{13/2}\rightarrow{}^4S_{3/2}$	0.0	-1621	1.1E-03	3.8E-01	2.3E+00	0.0E+00	6.3E-11
17	$^4I_{13/2}\rightarrow{}^2H_{11/2}$	0.0	-2375	1.1E-06	2.2E-04	3.5E-03	9.7E-02	9.2E-14
18	$^4I_{13/2}\rightarrow{}^4F_{7/2}$	0.0	-3753	6.7E-19	6.3E-12	3.8E-11	0.0E+00	1.0E-21
19	$^4I_{13/2}\rightarrow{}^4F_{5/2}$	0.0	-5414	1.7E-36	4.6E-26	2.7E-25	0.0E+00	4.9E-36
20	$^4I_{13/2}\rightarrow{}^4F_{3/2}$	0.0	-5750	~0	9.1E-31	5.4E-30	0.0E+00	1.5E-39
21	$^4I_{13/2}\rightarrow{}^2H_{9/2}$	0.0	-7794	~0	1.2E-55	1.5E-54	3.5E-53	1.3E-65
22	$^4I_{13/2}\rightarrow{}^4G_{11/2}$	0.0	-9669	~0	2.3E-86	3.5E-85	9.5E-84	2.1E-96
23	$^4I_{13/2}\rightarrow{}^4G_{9/2}$	0.0	-10675	~0	3.1E-105	1.5E-103	5.9E-102	1.2E-115
24	$^4I_{11/2}\rightarrow{}^4I_{9/2}$	0.0	7999	~0	5.5E-59	3.6E-58	1.3E-57	1.2E-68
25	$^4I_{11/2}\rightarrow{}^4F_{9/2}$	0.0	5141	1.0E-20	7.1E-23	6.4E-22	9.6E-21	2.5E-33
26	$^4I_{11/2}\rightarrow{}^4S_{3/2}$	0.0	2013	3.4E-02	4.9E-03	2.9E-02	0.0E+00	2.9E-12
27	$^4I_{11/2}\rightarrow{}^2H_{11/2}$	0.2	1259	1.2E+03	2.6E+00	4.1E+01	1.1E+03	6.0E-10
28	$^4I_{11/2}\rightarrow{}^4F_{7/2}$	0.3	-119	2.4E+03	1.6E+02	1.0E+03	3.0E+03	1.8E-08
29	$^4I_{11/2}\rightarrow{}^4F_{5/2}$	0.0	-1780	5.6E-05	4.1E-02	2.4E-01	0.0E+00	1.9E-11
30	$^4I_{11/2}\rightarrow{}^4F_{3/2}$	0.0	-2116	3.7E-06	1.4E-02	8.1E-02	0.0E+00	1.1E-12
31	$^4I_{11/2}\rightarrow{}^2H_{9/2}$	0.0	-4160	4.4E-21	4.4E-15	7.0E-14	2.0E-12	9.7E-25
32	$^4I_{11/2}\rightarrow{}^4G_{11/2}$	0.0	-6035	~0	1.3E-33	8.0E-33	1.1E-32	1.0E-42

33	$^4I_{11/2}\rightarrow{}^4G_{9/2}$	0.0	-7041	~0	2.4E-45	6.2E-44	2.1E-42	4.3E-55
34	$^4I_{9/2}\rightarrow{}^4F_{9/2}$	0.0	7392	~0	2.7E-50	1.4E-48	5.7E-47	7.3E-60
35	$^4I_{9/2}\rightarrow{}^4S_{3/2}$	0.0	4264	8.4E-15	1.2E-15	7.2E-15	0.0E+00	1.5E-25
36	$^4I_{9/2}\rightarrow{}^2H_{11/2}$	0.0	3510	6.1E-07	6.5E-10	1.7E-08	5.9E-07	4.8E-20
37	$^4I_{9/2}\rightarrow{}^4F_{7/2}$	0.0	2132	1.1E+00	1.3E-02	1.0E-01	9.6E-01	9.8E-13
38	$^4I_{9/2}\rightarrow{}^4F_{5/2}$	10.1	471	7.5E+04	7.9E+01	2.1E+03	7.3E+04	1.1E-08
39	$^4I_{9/2}\rightarrow{}^4F_{3/2}$	0.1	135	8.9E+02	1.3E+02	7.6E+02	0.0E+00	1.8E-08
40	$^4I_{9/2}\rightarrow{}^2H_{9/2}$	0.0	-1909	6.6E-04	4.1E-03	1.6E-01	6.0E+00	6.9E-12
41	$^4I_{9/2}\rightarrow{}^4G_{11/2}$	0.0	-3784	3.4E-17	1.5E-12	6.6E-11	2.5E-09	6.3E-22
42	$^4I_{9/2}\rightarrow{}^4G_{9/2}$	0.0	-4790	1.4E-28	1.8E-21	3.9E-20	1.3E-18	4.8E-30
43	$^4F_{9/2}\rightarrow{}^4S_{3/2}$	0.0	7122	~0	2.0E-47	1.2E-46	0.0E+00	3.6E-56
44	$^4F_{9/2}\rightarrow{}^2H_{11/2}$	0.0	6368	3.2E-33	1.3E-36	7.9E-35	3.2E-33	1.3E-46
45	$^4F_{9/2}\rightarrow{}^4F_{7/2}$	0.0	4990	5.5E-20	1.0E-22	1.8E-21	5.3E-20	7.0E-32
46	$^4F_{9/2}\rightarrow{}^4F_{5/2}$	0.0	3329	9.3E-08	1.0E-08	6.1E-08	2.2E-08	7.0E-19
47	$^4F_{9/2}\rightarrow{}^4F_{3/2}$	0.0	2993	7.7E-07	1.1E-07	6.6E-07	0.0E+00	6.9E-17
48	$^4F_{9/2}\rightarrow{}^2H_{9/2}$	0.2	949	1.3E+03	5.3E+00	6.0E+01	1.3E+03	2.6E-09
49	$^4F_{9/2}\rightarrow{}^4G_{11/2}$	0.1	-926	9.5E+02	3.4E+01	2.0E+03	7.8E+04	2.9E-09
50	$^4F_{9/2}\rightarrow{}^4G_{9/2}$	0.0	-1932	1.4E-04	2.1E-03	4.6E-02	1.5E+00	5.7E-12
51	$^4S_{3/2}\rightarrow{}^2H_{11/2}$	0.0	9496	~0	3.6E-83	2.1E-82	0.0E+00	2.8E-93
52	$^4S_{3/2}\rightarrow{}^4F_{7/2}$	0.0	8118	~0	6.4E-62	3.8E-61	0.0E+00	1.9E-70
53	$^4S_{3/2}\rightarrow{}^4F_{5/2}$	0.0	6457	1.4E-35	7.9E-39	3.5E-37	1.4E-35	1.1E-47
54	$^4S_{3/2}\rightarrow{}^4F_{3/2}$	0.0	6121	4.5E-31	1.7E-34	1.1E-32	4.4E-31	1.1E-43
55	$^4S_{3/2}\rightarrow{}^2H_{9/2}$	0.0	4077	9.3E-15	1.3E-15	7.9E-15	0.0E+00	4.3E-24
56	$^4S_{3/2}\rightarrow{}^4G_{11/2}$	0.0	2202	2.9E-02	4.2E-03	2.5E-02	0.0E+00	5.1E-13
57	$^4S_{3/2}\rightarrow{}^4G_{9/2}$	0.0	1196	6.4E+01	9.2E+00	5.5E+01	0.0E+00	8.4E-10
58	$^2H_{11/2}\rightarrow{}^4F_{7/2}$	0.0	8872	~0	1.9E-72	3.6E-71	1.1E-69	1.7E-82
59	$^2H_{11/2}\rightarrow{}^4F_{5/2}$	0.0	7211	~0	1.1E-47	6.8E-47	0.0E+00	2.2E-57
60	$^2H_{11/2}\rightarrow{}^4F_{3/2}$	0.0	6875	~0	3.8E-45	2.3E-44	0.0E+00	6.4E-53
61	$^2H_{11/2}\rightarrow{}^2H_{9/2}$	0.0	4831	3.2E-18	1.1E-20	1.3E-19	3.1E-18	2.1E-30
62	$^2H_{11/2}\rightarrow{}^4G_{11/2}$	0.0	2956	5.7E-06	4.7E-07	2.8E-06	2.4E-06	1.1E-16
63	$^2H_{11/2}\rightarrow{}^4G_{9/2}$	0.0	1950	6.6E+00	5.4E-02	4.6E-01	6.1E+00	4.9E-12
64	$^4F_{7/2}\rightarrow{}^4F_{5/2}$	0.0	8589	~0	5.2E-68	1.3E-66	4.5E-65	7.4E-78
65	$^4F_{7/2}\rightarrow{}^4F_{3/2}$	0.0	8253	~0	2.9E-63	2.5E-62	3.3E-61	1.6E-72
66	$^4F_{7/2}\rightarrow{}^2H_{9/2}$	0.0	6209	7.3E-32	5.2E-35	1.9E-33	7.1E-32	1.0E-44
67	$^4F_{7/2}\rightarrow{}^4G_{11/2}$	0.0	4334	2.8E-13	2.8E-16	7.8E-15	2.7E-13	4.0E-26
68	$^4F_{7/2}\rightarrow{}^4G_{9/2}$	0.0	3328	3.6E-05	1.7E-08	8.8E-07	3.5E-05	7.1E-19
69	$^4F_{5/2}\rightarrow{}^4F_{3/2}$	0.0	9914		2.6E-91	1.1E-89	4.1E-88	6.4E-101
70	$^4F_{5/2}\rightarrow{}^2H_{9/2}$	0.0	7870	~0	1.5E-57	3.1E-56	9.8E-55	1.0E-66
71	$^4F_{5/2}\rightarrow{}^4G_{11/2}$	0.0	5995	9.8E-32	1.4E-32	8.4E-32	0.0E+00	2.9E-42
72	$^4F_{5/2}\rightarrow{}^4G_{9/2}$	0.0	4989	1.3E-18	7.5E-22	3.2E-20	1.2E-18	7.1E-32
73	$^4F_{3/2}\rightarrow{}^2H_{9/2}$	0.0	8206	~0	1.3E-62	7.6E-62	0.0E+00	8.3E-72
74	$^4F_{3/2}\rightarrow{}^4G_{11/2}$	0.0	6331	1.8E-35	2.6E-36	1.5E-35	0.0E+00	3.7E-46
75	$^4F_{3/2}\rightarrow{}^4G_{9/2}$	0.0	5325	4.8E-24	6.9E-25	4.1E-24	0.0E+00	3.9E-35

76	$^2H_{9/2} \rightarrow {}^4G_{11/2}$	0.0	8375	~0	2.6E-64	9.7E-63	3.6E-61	1.9E-74
77	$^2H_{9/2} \rightarrow {}^4G_{9/2}$	0.0	7369	~0	2.2E-50	6.8E-49	2.4E-47	1.5E-59
78	$^4G_{11/2} \rightarrow {}^4G_{9/2}$	0.0	9244	~0	5.8E-79	3.4E-78	0.0E+00	7.6E-89

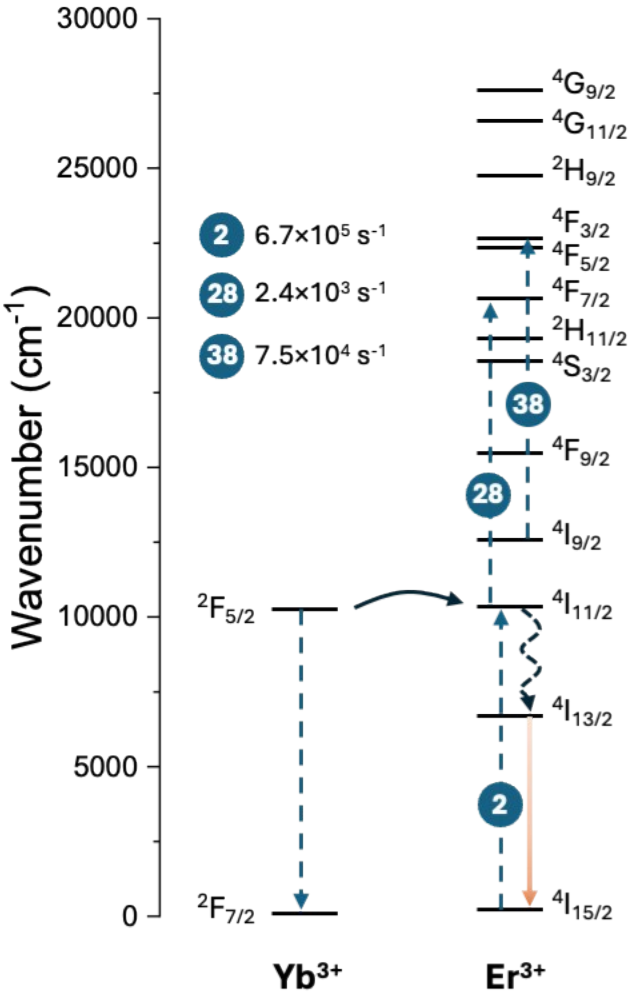

Figure S27. Partial energy level diagram showing only the three main Yb-Er interactions for the distance of 6.77 Å at 300 K. The labels correspond to the pathway number in Table S13.

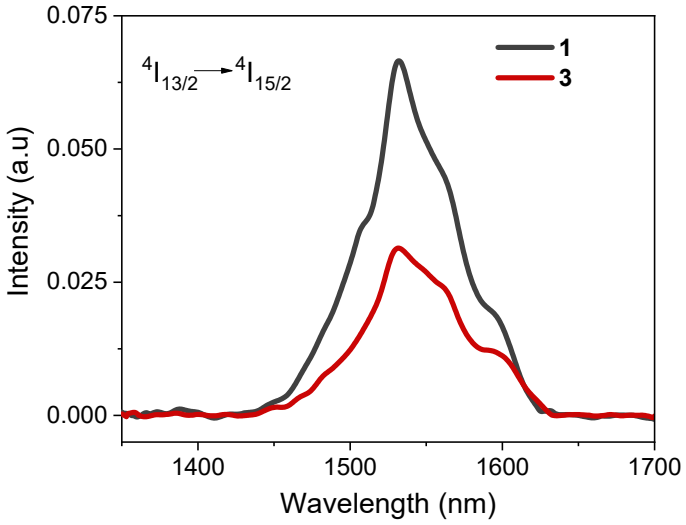

Figure S28. NIR emission spectrum for **1** and **3** at room temperature under 980 nm laser excitation.

5.2 Multireference *ab initio* calculations

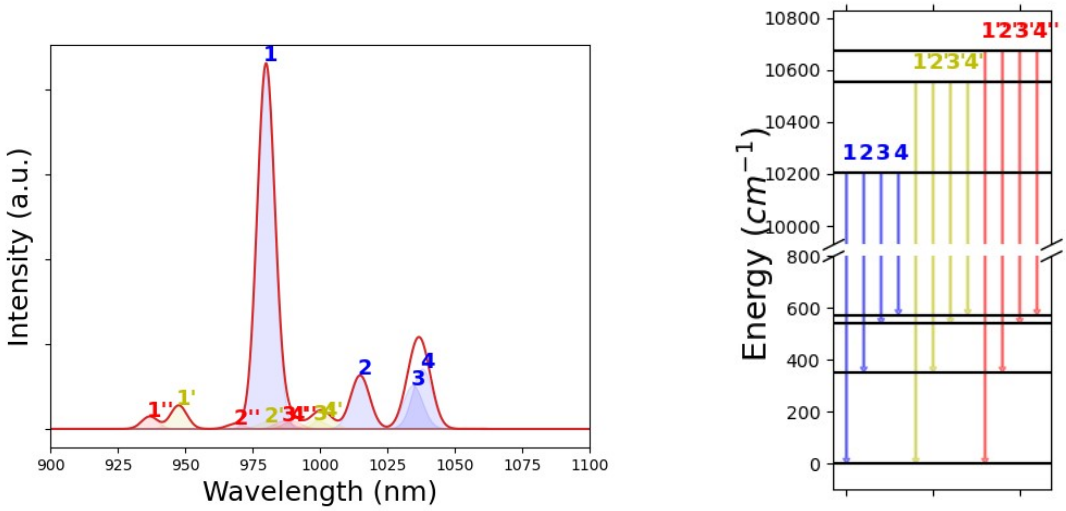

Figure S29. (Left) Decomposition of the $^2F_{5/2} \rightarrow {}^2F_{7/2}$ band in the contributions of each pair of Kramers' doublets for the Yb^{3+} centre from complex **1**. Presented data corresponds to a NEVPT2 calculation applied on top a CASSCF(13,14) calculation (see Theoretical section in the main text for further information). (Right) Corresponding calculated Dieke diagram for the Yb^{3+} centre. Blue, yellow and red colours indicate emission stemming from the V_1, V_2 and V_3 components of $^2F_{5/2}$ level, respectively.

References

1. L. K. Soro, R. C. Knighton, F. Avecilla, W. Thor, F. Przybilla, O. Jeannin, D. Esteban-Gomez, C. Platas-Iglesias and L. J. Charbonnière, *Adv. Optical Mater.*, 2023, **11**, 2202307.
2. D. Aguilà, V. Velasco, L. A. Barrios, J. González-Fabra, C. Bo, S. J. Teat, O. Roubeau and G. Aromí, *Inorg. Chem.*, 2018, **57**, 8429-8439.
3. L. Abad Galán, D. Aguilà, Y. Guyot, V. Velasco, O. Roubeau, S. J. Teat, M. Massi and G. Aromí, *Chem. Eur. J.*, 2021, **27**, 7288-7299.
4. J. Mooney and P. Kambhampati, *J. Phys. Chem. Lett.*, 2013, **4**, 3316-3318.
5. M. J. Frisch, G. W. Trucks, H. B. Schlegel, G. E. Scuseria, M. A. Robb, J. R. Cheeseman, G. Scalmani, V. Barone, G. A. Petersson, H. Nakatsuji, X. Li, M. Caricato, A. V. Marenich, J. Bloino, B. G. Janesko, R. Gomperts, B. Mennucci, H. P. Hratchian, J. V. Ortiz, A. F. Izmaylov, J. L. Sonnenberg, Williams, F. Ding, F. Lipparini, F. Egidi, J. Goings, B. Peng, A. Petrone, T. Henderson, D. Ranasinghe, V. G. Zakrzewski, J. Gao, N. Rega, G. Zheng, W. Liang, M. Hada, M. Ehara, K. Toyota, R. Fukuda, J. Hasegawa, M. Ishida, T. Nakajima, Y. Honda, O. Kitao, H. Nakai, T. Vreven, K. Throssell, J. A. Montgomery Jr., J. E. Peralta, F. Ogliaro, M. J. Bearpark, J. J. Heyd, E. N. Brothers, K. N. Kudin, V. N. Staroverov, T. A. Keith, R. Kobayashi, J. Normand, K. Raghavachari, A. P. Rendell, J. C. Burant, S. S. Iyengar, J. Tomasi, M. Cossi, J. M. Millam, M. Klene, C. Adamo, R. Cammi, J. W. Ochterski, R. L. Martin, K. Morokuma, O. Farkas, J. B. Foresman and D. J. Fox, *Wallingford, CT*, 2016.
6. Y. Zhao and D. G. Truhlar, *Theor. Chem. Acc.*, 2008, **120**, 215-241.
7. Y. Zhao and D. G. Truhlar, *J. Chem. Phys.*, 2006, **125**, 194101.
8. A. Schäfer, H. Horn and R. Ahlrichs, *J. Chem. Phys.*, 1992, **97**, 2571-2577.
9. M. Dolg, H. Stoll, A. Savin and H. Preuss, *Theor. Chim. Acta*, 1989, **75**, 173-194.
10. M. Dolg, H. Stoll and H. Preuss, *J. Chem. Phys.*, 1989, **90**, 1730-1734.
11. R. T. Moura, M. Quintano, C. V. Santos-Jr, V. A. C. A. Albuquerque, E. C. Aguiar, E. Kraka and A. N. Carneiro Neto, *Optical Materials: X*, 2022, **16**, 100216.
12. B. S. D. Onishi, A. N. Carneiro Neto, R. Bortolleto-Santos, V. R. Masterlaro, L. D. Carlos, R. A. S. Ferreira and S. J. L. Ribeiro, *Nanoscale*, 2024, **16**, 6286-6295.
13. S. S. Nobre, P. P. Lima, L. Mafra, R. A. Sá Ferreira, R. O. Freire, L. Fu, U. Pischel, V. de Zea Bermudez, O. L. Malta and L. D. Carlos, *J. Phys. Chem. C*, 2007, **111**, 3275-3284.
14. W. M. Faustino, O. L. Malta and G. F. de Sá, *J. Chem. Phys.*, 2005, **122**, 54109.
15. O. L. Malta, *J. Lumin.*, 1997, **71**, 229-236.
16. A. N. Carneiro Neto, E. E. S. Teotonio, G. F. de Sá, H. F. Brito, J. Legendziewicz, L. D. Carlos, M. C. F. C. Felinto, P. Gawryszewska, R. T. Moura, R. L. Longo, W. M. Faustino and O. L. Malta, in *Handbook on the Physics and Chemistry of Rare Earths*, eds. J.-C. G. Bünzli and V. K. Pecharsky, Elsevier, 2019, vol. 56, pp. 55-162.
17. E. Kasprzycka, A. N. Carneiro Neto, V. A. Trush, L. Jerzykiewicz, V. M. Amirkhanov, O. L. Malta, J. Legendziewicz and P. Gawryszewska, *J. Rare Earths*, 2020, **38**, 552-563.
18. A. N. Carneiro Neto, E. Mamontova, A. M. P. Botas, C. D. S. Brites, R. A. S. Ferreira, J. Rouquette, Y. Guari, J. Larionova, J. Long and L. D. Carlos, *Adv. Optical Mater.*, 2022, **10**, 2101870.
19. O. L. Malta, *Chem. Phys. Lett.*, 1982, **87**, 27-29.
20. O. L. Malta, *Chem. Phys. Lett.*, 1982, **88**, 353-356.
21. W. T. Carnall, H. Crosswhite and H. M. Crosswhite, *Energy level structure and transition probabilities in the spectra of the trivalent lanthanides in LaF_3*, Argonne National Lab. (ANL), Argonne, IL (United States), United States, 1978.
22. T. Kushida, *J. Phys. Soc. Jpn.*, 1973, **34**, 1318-1326.
23. E. Kasprzycka, A. N. Carneiro Neto, V. A. Trush, O. L. Malta, L. Jerzykiewicz, V. M. Amirkhanov, J. Legendziewicz and P. Gawryszewska, *Spectrochim. Acta A Mol. Biomol. Spectrosc.*, 2022, **274**, 121072.

24. S. Edvardsson and M. Klintenberg, *J. Alloys Compd.*, 1998, **275-277**, 230-233.
25. A. N. Carneiro Neto and R. T. Moura Jr, *Chem. Phys. Lett.*, 2020, **757**, 137884.
26. O. L. Malta, *J. Non-Cryst. Solids*, 2008, **354**, 4770-4776.
27. O. L. Malta and F. R. Gonçalves e Silva, *Spectrochim. Acta A Mol. Biomol. Spectrosc.*, 1998, **54**, 1593-1599.
28. O. L. Malta, H. F. Brito, J. F. S. Menezes, F. R. G. e. Silva, S. Alves, F. S. Farias and A. V. M. de Andrade, *J. Lumin.*, 1997, **75**, 255-268.
29. A. N. Carneiro Neto, R. T. Moura, Jr., A. Shyichuk, V. Paterlini, F. Piccinelli, M. Bettinelli and O. L. Malta, *J. Phys. Chem. C*, 2020, **124**, 10105-10116.